



## RESEARCH ARTICLE

10.1029/2019MS001671

# Local and Remote Controls on Arctic Mixed-Layer Evolution

**Key Points:**

- Lagrangian LES of Arctic cloudy mixed layers in evolving warm air masses is constrained by in situ observations from the PASCAL field campaign
- A novel iterative method relying on LES on microgrids is applied to optimize the case configuration and adjust biases in GCM-derived forcings
- Budget studies give insight into local and remote controls on AML evolution, suggesting large-scale subsidence events can cause low-level cloud collapse over the sea ice

**Correspondence to:**

R. A. J. Neggers,  
neggers@meteo.uni-koeln.de

**Citation:**

Neggers, R. A. J., Chylik, J., Egerer, U., Griesche, H., Schemann, V., Seifert, P., et al. (2019). Local and remote controls on Arctic mixed-layer evolution. *Journal of Advances in Modeling Earth Systems*, 11, 2214–2237. <https://doi.org/10.1029/2019MS001671>

Received 27 FEB 2019

Accepted 29 MAY 2019

Accepted article online 17 JUN 2019

Published online 11 JUL 2019

©2019. The Authors.

This is an open access article under the terms of the Creative Commons Attribution-NonCommercial-NoDerivs License, which permits use and distribution in any medium, provided the original work is properly cited, the use is non-commercial and no modifications or adaptations are made.

R. A. J. Neggers<sup>1</sup> , J. Chylik<sup>1</sup>, U. Egerer<sup>2</sup> , H. Griesche<sup>2</sup> , V. Schemann<sup>1</sup> , P. Seifert<sup>2</sup> ,  
H. Siebert<sup>2</sup> , and A. Macke<sup>2</sup> 

<sup>1</sup>Institute for Geophysics and Meteorology, University of Cologne, Cologne, Germany, <sup>2</sup>Leibniz Institute for Tropospheric Research (TROPOS), Leipzig, Germany

**Abstract** In this study Lagrangian large-eddy simulation of cloudy mixed layers in evolving warm air masses in the Arctic is constrained by in situ observations from the recent PASCAL field campaign. A key novelty is that time dependence is maintained in the large-scale forcings. An iterative procedure featuring large-eddy simulation on microgrids is explored to calibrate the case setup, inspired by and making use of the typically long memory of Arctic air masses for upstream conditions. The simulated mixed-phase clouds are part of a turbulent mixed layer that is weakly coupled to the surface and is occasionally capped by a shallow humidity layer. All eight simulated mixed layers exhibit a strong time evolution across a range of time scales, including diurnal but also synoptic fingerprints. A few cases experience rapid cloud collapse, coinciding with a rapid decrease in mixed-layer depth. To gain insight, composite budget analyses are performed. In the mixed-layer interior the heat and moisture budgets are dominated by turbulent transport, radiative cooling, and precipitation. However, near the thermal inversion the large-scale vertical advection also contributes significantly, showing a distinct difference between subsidence and upsidence conditions. A bulk mass budget analysis reveals that entrainment deepening behaves almost time-constantly, as long as clouds are present. In contrast, large-scale subsidence fluctuates much more strongly and can both counteract and boost boundary-layer deepening resulting from entrainment. Strong and sudden subsidence events following prolonged deepening periods are found to cause the cloud collapses, associated with a substantial reduction in the surface downward longwave radiative flux.

## 1. Introduction

The exchange of air masses between the Arctic and midlatitudes has been identified as a key process in the ongoing warming of the Arctic climate (Pithan et al., 2018; Sedlar & Tjernström, 2017; Turner & Gyakum, 2011). Warm air intrusions (Johansson et al., 2017; Kapsch et al., 2013; Woods & Caballero, 2016; Woods et al., 2013) typically feature low-level clouds in mixed phase that are part of a well-mixed turbulent layer (e.g., Curry et al., 2000; de Boer et al., 2011; McFarquhar et al., 2011; Shupe, 2011; Shupe et al., 2006; Tjernström et al., 2015; Verlinde et al., 2007). The gradual transition toward a cloud-free state is associated with a large change in the surface radiative energy budget (Bennartz et al., 2012; Curry et al., 1996; Miller et al., 2015), which can in turn significantly affect sea ice melt (Kapsch et al., 2016). The persistent and widespread occurrence of mixed-phase clouds in the Arctic thus makes them an important component of the local climate system (Morrison et al., 2012). Arctic low-level clouds in general are not optimally represented in weather and climate models (Pithan et al., 2014, 2016; Svensson & Karlsson, 2011), and linking this problem to climate sensitivity is the subject of intense ongoing research (Holland & Bitz, 2003; Tan et al., 2016).

For these reasons the cloudy Arctic mixed layer (AML) has been intensely studied in recent decades. The processes controlling its evolution cover a broad range of scales (e.g., Curry et al., 1997). In addition, a distinction can be made between locally driven processes and more remotely controlled processes (Tjernström et al., 2019). Local processes act mostly on small scales and include the surface exchange of heat and humidity, vertical mixing by turbulence driven by cloud top cooling (Shupe et al., 2013), the microphysics of mixed-phase clouds and their sensitivity to condensation nuclei (Ovchinnikov et al., 2011; Solomon et al., 2011), and the degree of coupling of the AML to the surface (e.g., Brooks et al., 2017; Solomon et al., 2014, 2015). In contrast, remotely controlled processes act on much larger scales and are related to large-scale dynamics. Horizontal advection by the air mass supplies remotely sourced heat and moisture, while the

kinematic state of the AML is affected by pressure gradients and wind shear. Large-scale subsidence is effective in reducing the depth of the AML. The correlation between cloudy/radiative states and surface pressure as reported by Stramler et al. (2011) and Morrison et al. (2012) further emphasizes the strong link between cloud occurrence and synoptic activity.

How exactly local and remotely controlled processes cooperate to establish the mixed-layer evolution and the associated cloud transition is still not fully understood. One of the complications is that budget studies are required to gain more insight into their relative roles; however, the direct measurement of these individual terms is notoriously difficult. In recent years high-resolution simulations are increasingly used to virtually fill this data gap. Large-eddy simulation (LES) including microphysics representations can provide virtual fully four-dimensional information about all processes acting on the air mass and thus supplement observations. Typically, LES experiments are based on measurements at fixed sites or during field campaigns, with the simulations being critically interpreted and evaluated (Fridlind et al., 2012; Klein et al., 2009; Morrison et al., 2011; Ovchinnikov et al., 2014). In recent years LES of mixed-phase clouds in warm air intrusions is increasingly being pursued and is yielding valuable new insights (Loewe et al., 2017; Savre & Ekman, 2015; Savre et al., 2015; Sotiropoulou et al., 2018).

LES studies based on observed data are often slightly idealized, in order to remove irrelevant complexity and thus make the scientific problem more transparent. This concerns (i) smoothed initial profiles, (ii) spatially homogeneous forcing, and (iii) periodic boundary conditions. On the other hand, oversimplification can remove complexity that is actually of key importance. For Arctic application this concerns two particular simplifications. The first is the often-made assumption of time-constant large-scale forcings, which might remove important fluctuations that affect the mixed-layer evolution. The second assumption is the adoption of a Eulerian frame of reference, fixed at one location. This is conceptually not compatible with the typically long life cycle of ice hydrometeors (Westbrook & Illingworth, 2013), as well as the smallness of the turbulent energy budget during the summer melt season (Brooks et al., 2017). These two characteristics effectively give the AML a “long memory” of upstream conditions. In Eulerian domains these effects have to be represented in the prescribed lateral inflow, while ideally they should be allowed to act freely and for a long enough time.

Adopting a domain that follows the flow in principle can partially address some of these problems. For example, Lagrangian configurations have successfully been applied in many single-column model and LES studies of warm cloud transitions in the subtropics (Bretherton et al., 1999; Neggers et al., 2017; Van der Dussen et al., 2013). While it has also long been used for interpreting observed Arctic air mass behavior (Curry, 1983; Wexler, 1936), only recently was it first applied in single-column model studies in the area (Pithan et al., 2016). A practical complication for Lagrangian LES in the Arctic is the absence of permanently operating dense measurement networks. This means that air masses are typically only sampled once, at one point in space and time. It also means that analyses and forecasts by general circulation models (GCM) feature significant and persistent biases at low levels over the sea ice (Jakobson et al., 2012; Lindsay et al., 2014), which complicates the use of analysis data for constructing boundary conditions and forcings for small-domain LES studies in the area. How to best constrain Lagrangian LES experiments of observed Arctic air masses in poorly sampled areas is therefore still an open research question.

The main objective of this study is to explore new ways to configure and constrain Lagrangian LES realizations of Arctic mixed-phase clouds in warm air intrusions and to use these simulations as a virtual laboratory for gaining more insight into the relative role of local versus remote controls on the AML development. A key novelty is that full time dependence is maintained in the large-scale forcings. Second, a new method is explored for estimating the upstream initial conditions that makes use of LES on microgrids, as part of an iterative reverse-engineering approach to adjust biases in GCM-derived forcings. This method is inspired by and makes use of the typically long memory of Arctic air masses.

In practice a set of eight independent Lagrangian cases is configured, reflecting intruding warm air masses over the sea ice as probed by the *Polarstern* research cruise PS106.1 in early June 2017 in the sea ice north of the Svalbard Archipelago, as part of the PASCAL (Physical feedbacks of Arctic planetary boundary layer, Sea ice, Cloud And Aerosol: PS106/1) field campaign (Macke & Flores, 2018). All cases are calibrated against two independent observational data sets that reflect the bulk AML state. The subsequent simulations are evaluated against a further eight independent observational data sets that reflect the thermodynamic, kinematic, and cloudy state of the AML. Budget studies of AML thermodynamics and bulk mass based on these

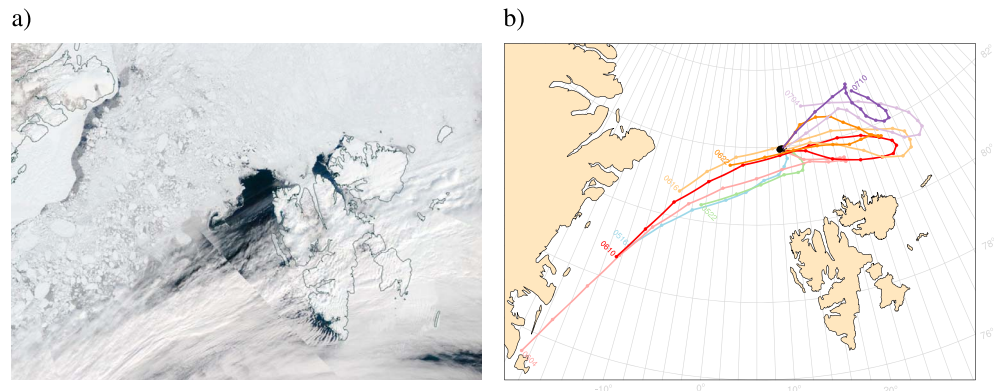


**Figure 1.** (a) MODIS Aqua satellite image (corrected reflectance, true color) of the area around Svalbard on 6 June 2017. Image courtesy of NASA EOSDIS Worldview. (b) Overview of all eight back trajectories simulated in this study, as listed in Table 2. The starting points of each trajectory are marked by its case ID, while their end point (the *Polarstern*) is indicated by the black dot. The land mass is shaded yellow.

simulations are then performed to identify controlling processes in the AML evolution. Of particular interest is the question to what extent fluctuations in the large-scale subsidence can modulate low-level cloud amount.

Section 2 describes both the model data and observational data sets used in this study. The method for configuring the Lagrangian cases and performing the simulations is documented in section 3. The results are discussed in section 4, while their implications are further discussed in section 5. Section 6 provides a brief summary of the main conclusions and gives an outlook on further research.

## 2. Models and Measurements

### 2.1. The PASCAL Field Campaign

The PASCAL field campaign (Macke & Flores, 2018) took place in the vicinity of the Svalbard Archipelago in May and June 2017. PASCAL and its sister campaign ACLOUD (Arctic CLOUD Observations Using airborne measurements during polar Day) were organized as part of the ongoing (AC)<sup>3</sup> research program (Wendisch et al., 2017). At the center of PASCAL is the *Polarstern* research vessel (PS, Knust, 2017), carrying instrumentation for measuring near-surface meteorology, turbulence, radiation, clouds and aerosol. Collocated measurements were performed by two research aircraft from the ACLOUD campaign (Wendisch et al., 2018). The PS was attached to an ice floe from 4–16 June, on which a network of additional instrumentation was installed and operated.

The period of interest for this study is 5–7 June 2017, when the PS was located in the sea ice at approximately 81.9°N, 10.9°E. The ice and cloud situation on 6 June 2017 is shown in Figure 1. As described by Knudsen et al. (2018) and Wendisch et al. (2018), on these days surface pressure was relatively high in the area, and low clouds were predominantly single layer and in mixed phase. The low-level flow was initially from the southwest, bringing relatively warm and moist air masses into the area. During this period the flow gradually changed into an east-northeasterly, as can be seen in Figure 1a from Lee waves in the cloud deck triggered by the Svalbard topography.

Table 1 gives an overview of the observations used in this study, including information on the data stream and the associated instrument. For a more detailed description we refer to Macke and Flores (2018).

### 2.2. Analyses and Short-Range Forecasts

The large-scale data used in this study to estimate the forcings and boundary conditions for the LES experiments is obtained from the Integrated Forecasting System (IFS) of the European Centre for Medium-range Weather Forecasts (ECMWF). To optimize the time frequency of the forcing data set, a combination is used for analyses (available every 12 hr) and short-range forecasts (available at 3-hourly time-points in between). The time span of these forecasts is assumed to be short enough to minimize forecast drift. Their combination effectively yields a four-dimensional data set of the atmospheric state variables at 3-hourly temporal resolution, and  $0.1 \times 0.1^\circ$  spatial resolution. While the ECMWF data form the basis of the forcings, adjustments are made to correct biases, as described in detail in section 3.2.

**Table 1**

Overview of the PASCAL Observational Data Sets Used in This Study, as Collected by Instrumentation on Board the Polarstern Research Vessel

Variable	Unit	Description	Dimensionality	Instrument
$q_v$	kg/kg	Water vapor specific humidity	$(z, t)$	Radiosonde
$\theta_v$	K	Virtual potential temperature	$(z, t)$	Radiosonde
$z_i$	m	Thermal inversion height	$(t)$	Radiosonde
$T_{29}$	K	Temperature at 29 m	$(t)$	Thermometer
$p_s$	hPa	Air pressure at surface	$(t)$	Barometer
RH <sub>29</sub>	%	Relative humidity at 29 m	$(t)$	Hygrometer
$U_{39}$	m/s	Wind speed at 39 m	$(t)$	Anemometer
$\alpha_{39}$	°	Wind direction at 39 m	$(t)$	Anemometer
$z_b$	m	Liquid cloud base height	$(t)$	Ceilometer
$z_t$	m	Liquid cloud top height	$(t)$	Radar
LWC <sub>max</sub>	kg/m <sup>3</sup>	Maximum liquid cloud water content	$(t)$	MWR
IWC <sub>max</sub>	kg/m <sup>3</sup>	Maximum ice cloud water content	$(t)$	MWR
SW <sub>d</sub>	W/m <sup>2</sup>	Surface short wave downward radiative flux	$(t)$	Pyranometer

Note. All data are available at the PANGAEA<sup>a</sup> database.

<sup>a</sup>Surface meteorology, ceilometer and radiation: <https://doi.org/10.1594/PANGAEA.886302>. Radiosondes: <https://doi.org/10.1594/PANGAEA.882736>.

### 2.3. LES

The LES simulations in this study are performed with the Dutch Atmospheric Large-Eddy Simulation code (DALES, Heus et al. (2010)). This code has been successfully used in previous studies to simulate various regimes of moist atmospheric convection including precipitating stratocumulus and has taken part in recent LES intercomparison studies on this cloud regime (de Roode et al., 2016; Van der Dussen et al., 2013). To enable the simulation of Arctic clouds, the double-moment mixed-phase microphysics scheme of Seifert and Beheng (2006) was newly implemented. Five hydrometeor species are represented, including suspended cloud hydrometeors in liquid and frozen states and precipitating hydrometeors in the form of rain, snow, and graupel. The cloud condensation nuclei concentration is prognostic in the simulations, while the ice nucleation particles concentration is constant. Both are initialized using reference climatological values for the Arctic. For the calculation of the vertical transfer of radiative energy a Monte Carlo Spectral Integration technique is used. Resolved advection is calculated with a centered-difference scheme, while subgrid transport is represented with a prognostic turbulent kinetic energy scheme. For the time integration a Runge-Kutta

**Table 2**

Details of the Eight Trajectories Simulated in This Study

Case ID	PS date (dd/mm/yyyy)	PS time (UTC)	Radiosonde ID	Initial Latitude (°N)	Initial Longitude (°E)	Duration (hr)	Distance (km)
0516	05/06/2017	16:50	882680	78.97	-11.54	30	556.6
0522	05/06/2017	22:41	882681	80.42	-2.68	30	399.6
0604	06/06/2017	04:32	882682	75.44	-18.90	54	1,307.6
0610	06/06/2017	10:52	882683	78.60	-12.68	54	1,260.7
0616	06/06/2017	16:52	882684	80.67	-6.43	54	1,125.6
0622	06/06/2017	22:49	882685	81.52	1.32	54	788.0
0704	07/06/2017	04:33	882686	82.99	15.27	54	853.8
0710	07/06/2017	10:48	882687	83.03	26.55	54	593.5

Note. The first column is the ID of the Lagrangian case as used in this study, its four digits consisting of the day (column 2) and hour (column 3) of the arrival of the air mass at the PS. The arrival coincides with the radiosonde launches (column 4), indicated by the ID as used in the PANGAEA database<sup>a</sup>. The last four columns reflect the initiation coordinates, the duration of the simulation, and the distance travelled by the air mass. PS = *Polarstern*.

<sup>a</sup><https://doi.org/10.1594/PANGAEA.<ID>>

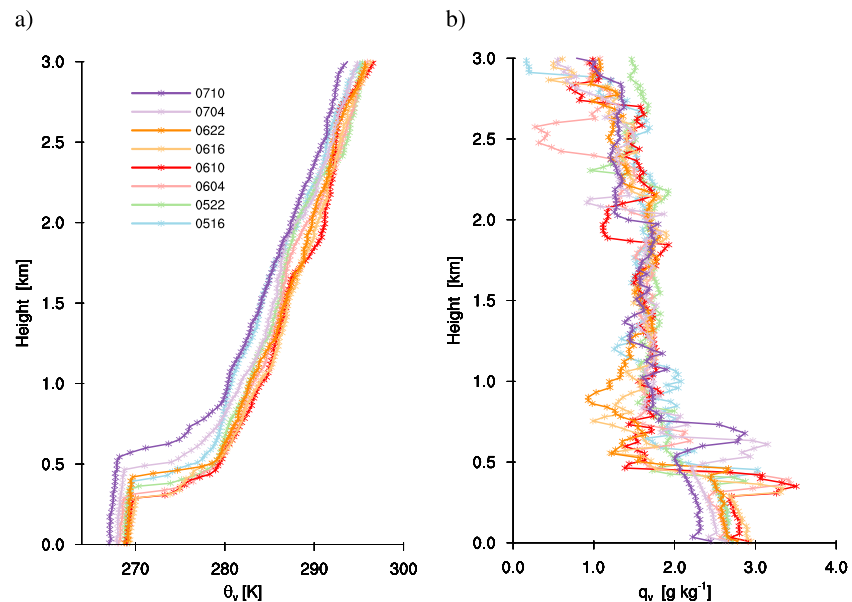


**Figure 2.** Vertical profiles of (a) virtual potential temperature  $\theta_v$  and (b) water vapor specific humidity  $q_v$  from eight radiosondes launched from the *Polarstern* during the period 5–7 June 2017. Each radiosonde is labeled with the case ID as given in Table 2 and is indicated by a unique color. This color is consistent with the trajectories plotted in Figure 1b and with other figures showing multiple case results.

scheme is applied. For any further details about DALES we refer to Heus et al. (2010). The standard DALES code is publicly available online (<https://github.com/dalesteam/dales>).

### 3. Method

#### 3.1. Back Trajectories

The first step in configuring a Lagrangian case is to estimate the movement of the air mass of interest. To this purpose back trajectories are calculated from the ECMWF data. Radiosonde launches at the PS within the period of interest are used as the starting location and time of the back trajectory calculation. From that point the movement of the air mass at 950 hPa is reconstructed in upstream direction for 2 days. With four radiosondes launched on each day at roughly 6-hr intervals, this yields eight back trajectories, with their details summarized in Table 2. In principle all simulations start from a point 2 days upstream from the PS and then follow the air masses as it moves ever closer. Exceptions to this rule are the first two cases which start only 1 day upstream from the PS, in order to exclude time periods when the air mass was situated over Greenland.

Figure 2 shows the vertical structure of virtual potential temperature  $\theta_v$  and water vapor specific humidity  $q_v$  for all eight radiosondes that were used as the starting point for back trajectory calculation. These launches cover a time period from noon 5 June 2017 to noon 7 June 2017. Within this period a cloudy mixed layer existed continuously, situated below a thermal inversion at a height varying between 250 and 600 m. This variation in height was the main motivation for selecting this time period for our study, as it makes the eight cases span a reasonably broad parameter space of AML states. Another reason was the persistent presence of a capping humidity layer during this period (Brunke et al., 2015; Naakka et al., 2018), identified as a key research topic in the (AC)<sup>3</sup> project.

#### 3.2. Initialization, Forcing, and Boundary Conditions

The initial state, large-scale forcings, and boundary conditions along the trajectories are all derived from the ECMWF data. These data are available through the online data repository as mentioned in the acknowledgments. Both the forcings and boundary conditions are fully time dependent, unless stated otherwise below. A key step is to correct critical biases in the initial state as derived from the GCM data, using in situ observations by the PS. The guiding principle in making these adjustments is that the LES should reproduce the bulk AML depth and thermodynamic state when it arrives at the PS, while the turbulence and clouds are still free to evolve during the simulations.

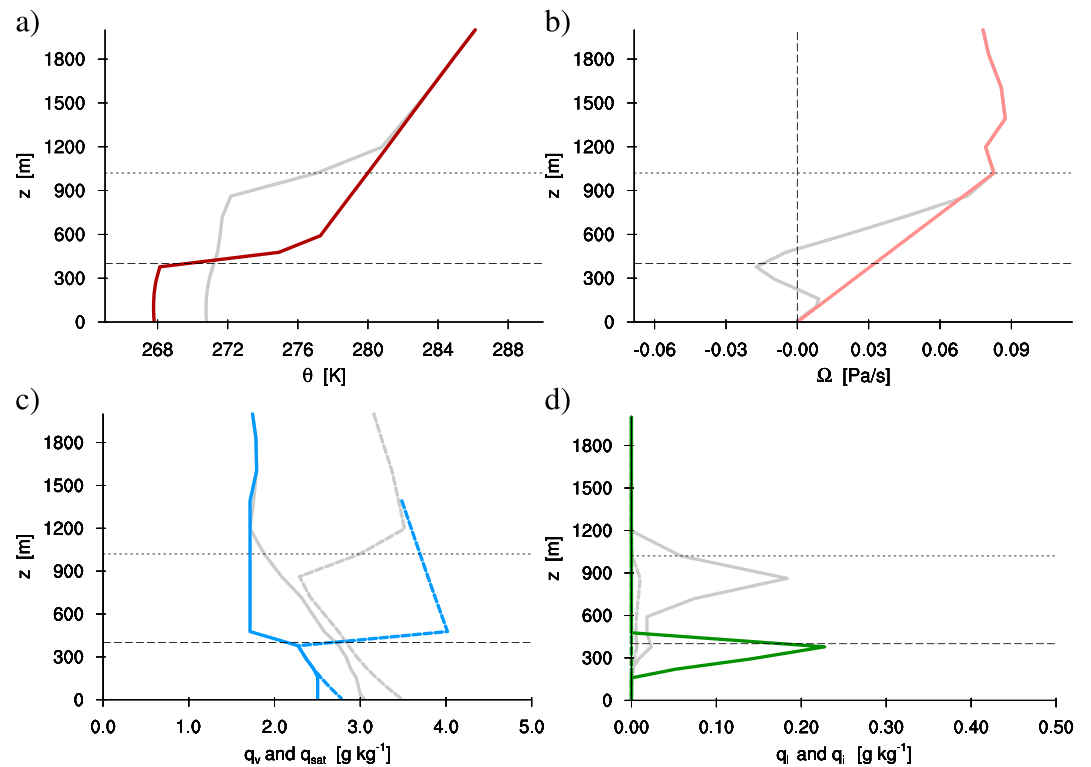


**Figure 3.** Modifications in the ECMWF IFS-derived initial state for the 0704 case. (a) Potential temperature  $\theta$ , (b) prescribed large-scale subsidence/lifting  $\Omega$ , (c) water vapor specific humidity  $q_v$  and saturation specific humidity  $q_{\text{sat}}$  (dashed), and (d) cloud liquid condensate  $q_l$  and ice condensate  $q_i$  (dashed). The ECMWF IFS data are plotted in gray, while the adjusted initial state is shown in color. The two horizontal black lines represent the original inversion height  $z_i$  (dotted) and the adjusted inversion height  $z_{i0}$  (dashed). ECMWF = European Centre for Medium-range Weather Forecasts; IFS = Integrated Forecasting System.

### 3.2.1. Boundary Conditions

Prescribed surface boundary conditions include the skin temperature and the roughness lengths for heat and momentum. The skin temperature is calculated as the area-weighted sum of the open sea surface temperature (SST) and the sea ice temperature in the ECMWF model; because the sea ice fraction is large in all cases ( $> 0.9$ , not shown), the skin temperature effectively reflects that of the sea ice. The surface fluxes of heat, moisture, and momentum are all interactively calculated using surface layer similarity, depending on the atmosphere-surface difference and low-level wind speed. Surface evaporation depends on skin layer saturation humidity values. At the top of the atmosphere the solar insolation is prescribed, depending on time of day, location, and season. This means a diurnal cycle in the radiative energy budget can be expected in the simulations.

### 3.2.2. Lagrangian Forcing

This study adopts the method of deriving large-scale forcings for the state variables  $(U, V, \theta_l, q_l)$  from the ECMWF data as described in detail by Van Laar et al. (2019). In the simulations horizontal advective forcing is represented through prescribed advective tendencies. First these tendencies are calculated at each grid point within a  $0.5^\circ \times 0.5^\circ$ -wide column around the location of interest. Horizontal averaging then yields a vertical profile of tendencies. We deviate from this method only at two key points:

1. The forcings are estimated at points along the trajectories instead of at a fixed location.
2. The wind velocity at 950 hPa is subtracted from the wind profiles in the calculation of the prescribed horizontal advective tendencies.

In effect this step yields a “demi-Lagrangian” advective forcing tendency, in that it is negligible within the AML but nonnegligible above.

Vertical large-scale advection is represented using a prescribed subsidence profile, by which advection becomes interactive with the simulated vertical gradients. As illustrated in Figure 3b, the subsidence profile

is linearized between the thermal inversion  $z_i$  and the surface. This corresponds to assuming a constant large-scale divergence within that height range, a configuration often applied in LES of low cloud transitions (e.g., Loewe et al., 2017; Neggers et al., 2017; Sandu & Stevens, 2011; Sotiropoulou et al., 2018). One of the main reasons for adopting it here is that the linearization effectively removes any fingerprints of the parameterized boundary layer in the ECMWF model, which should be resolved by the LES itself. Inversion height  $z_i$  is calculated as the height at which the vertical gradient in  $\theta_v$  is strongest.

### 3.2.3. Initial State

Most operational circulation models used for weather forecasting and (re)analysis calculation persistently feature a too deep and warm boundary layer over the sea ice, with too weak thermal inversions (de Boer et al., 2014; Jakobson et al., 2012; Lindsay et al., 2014; Makshtas et al., 2007; Wesslén et al., 2014). To correct the initial profiles for this bias, an iterative procedure is applied that makes use of an ensemble of LES simulations on “microgrids,” consisting of only a limited number of adjacent grid columns. As demonstrated in Appendix A, at relatively small grid sizes the turbulence and entrainment is already resolved to a reasonable degree while still being computationally very efficient. Such microgrid configurations can thus function as glorified bulk mixed-layer models for calibrating cases, without the need for a parameterized top entrainment as used in classic bulk modeling.

The adjustment procedure consists of a sequence of steps, as illustrated by Figure 3:

1. A new inversion height  $z_{i0}$  is chosen.
2. Between a selected height  $z_{ep}$  and  $z_{i0}$  the  $\theta_v$  profile is extrapolated downward. At  $z_{ep} = 1,200$  m the extrapolation level is always situated above the AML top (see Figure 2), between which the lapse rate varies only weakly across cases.
3. For  $z_{i0} < z < z_{ep}$  the water vapor is set constant at the value at height  $z_{ep}$ , while all cloud is removed.
4. Below  $z_{i0}$  the potential temperature is modified uniformly by  $\Delta\theta_0$ . The prescribed skin temperature is similarly adjusted.
5. Below  $z_{i0}$  the specific humidity  $q_t$  is assumed constant with height and is tied to the new AML temperature structure by imposing a fixed relative humidity just below the new AML top. Assuming a value of 110% ensures the initial presence of some cloud mass, so that cloud radiative cooling can spin-up and maintain resolved turbulence from the start.
6. Below  $z_{i0}$  the new liquid cloud condensate mass is calculated as the difference  $q_t - q_{sat}$ , wherever positive, with saturation depending on the adjusted temperature. All other hydrometeor species are set to 0, their formation being assumed part of the model spin-up.

Using this procedure, a cluster of adjusted cases is constructed that covers a phase space of  $(z_{i0}, \Delta\theta_0)$  values. This allows searching for a combination that after time integration of a microgrid configuration for 48 hr yields an inversion height and low-level temperature that are as close as possible to the PS observations. This initial state is then adopted for the full macrogrid simulations. As will be shown in section 4.1, the long memory of the AML for upstream conditions is the main reason why this approach can be effective. Note that the initial profiles of wind are left unadjusted on purpose, due to the typical lack of a clear inversion in both wind speed and direction (not shown).

The initial state thus produced takes into account what might have happened with the air mass upstream of the PS. The guess is optimally informed by the PS measurements and takes into account the effect of processes including surface exchange, turbulent transport, entrainment deepening, microphysics, and large-scale forcing. The cases can thus best be interpreted as possible scenarios for the air mass development that are grounded in reality through calibration against downstream in situ data. Of course alternative scenarios might exist that yield a similar end state, for example, when using data from a different GCM. The availability of upstream measurements would be ideal for constraining these cases even further. Nevertheless, in the absence of the latter, the cases are already realistic enough to be useful for gaining insight into what controls their evolution, which is the main objective of this study.

### 3.3. Experiment Setup

Two types of LES grids are used in this study. The *microgrids* have a size of  $8 \times 8 \times 126$  and are discretized at  $100 \times 100 \times 10$ -m resolution, covering a domain size of 800 m in the horizontal. Experiments with these grids are primarily used for the optimization of the cases as described in the previous section 3.2. The *macrogrids* have a size of  $128 \times 128 \times 126$  and are much more finely discretized at  $20 \times 20 \times 10$  m. These grid sizes are

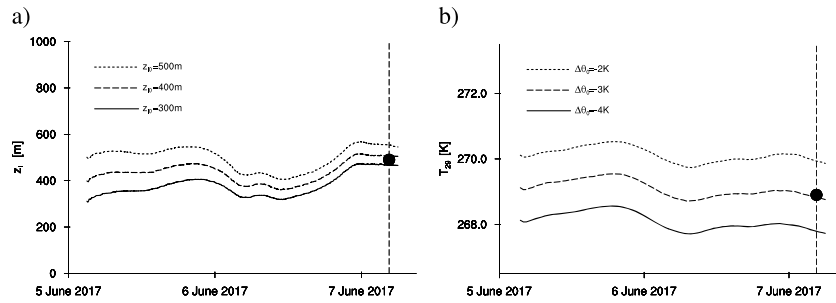


**Figure 4.** Sensitivity of bulk AML properties to initial conditions for the 0704 case. In panel (a) the time-evolution of the AML depth  $z_i$  during three experiments with a different initial depth  $z_{i0}$  are compared, while panel (b) compares the evolution of low-level temperature  $T_{29}$  of three experiments with differing initial AML potential temperature perturbation  $\Delta\theta_0$ . The time of the PS crossing is indicated by the vertical dashed line, while the associated PS observation is indicated by the black dot. AML = Arctic mixed layer; PS = *Polarstern*.

commonly used in many LES studies, while the high spatial resolution is required for resolving the weak turbulence in Arctic mixed layers under strong inversions. The same LES code is used for both grids.

Periodic horizontal boundaries are applied. The large-scale forcings are horizontally homogeneous but vary in time and with height. Continuous nudging is applied above 1,200 m at a 6-hr time scale while below the nudging is absent and the model state is completely free to develop. Nudging increases in intensity in the top quarter of the domain, in order to dampen spurious gravity waves. In principle the simulations cover the 48 hr before the air mass arrives at the PS. Surface sensible and latent heat fluxes are interactive, meaning that coupling between the AML and the surface can freely develop. Weak coupling is required for maintaining a sufficient supply of humidity to the mixed layer, so that cloud presence is maintained long enough. Use is made of prescribed climatological profiles of important greenhouse gases such as ozone, as input for the radiation scheme.

#### 4. Results

The presentation of the results is divided into two main parts. The first part focuses on the microgrid simulations, discussing their use in the case calibration and the evaluation against selected PS observations. The second part presents results with the macrogrids and how they are used to gain insight into local and remote controls on AML evolution.

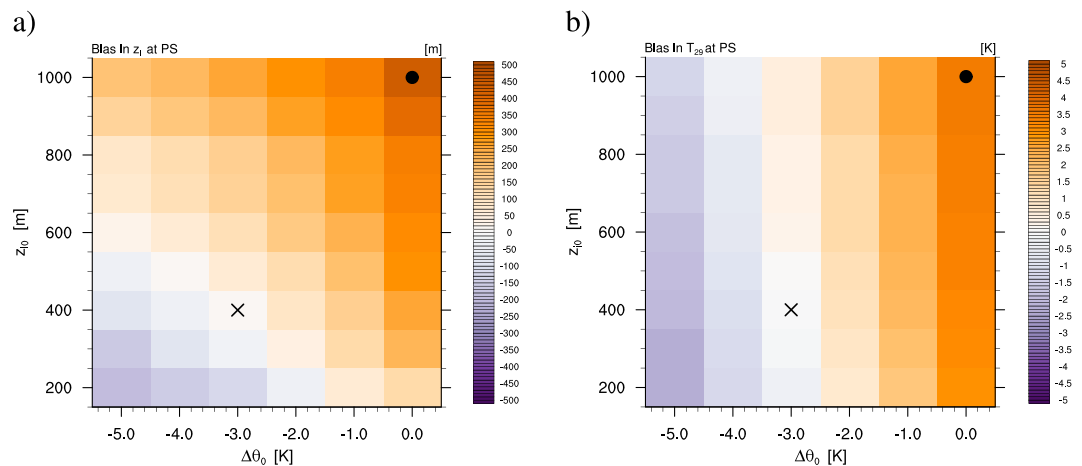


**Figure 5.** Phase space analysis of the dependence of the downstream bias relative to the PS measurements of (a) the inversion height  $z_i$  and (b) the low-level temperature  $T_{29}$  on the adjustments in the initial state, for the 0704 case. Each gridpoint represents one microgrid simulation. The black dot indicates the Integrated Forecasting System state, while the black cross marks the adjusted state finally adopted for the simulation in this study. PS = *Polarstern*.

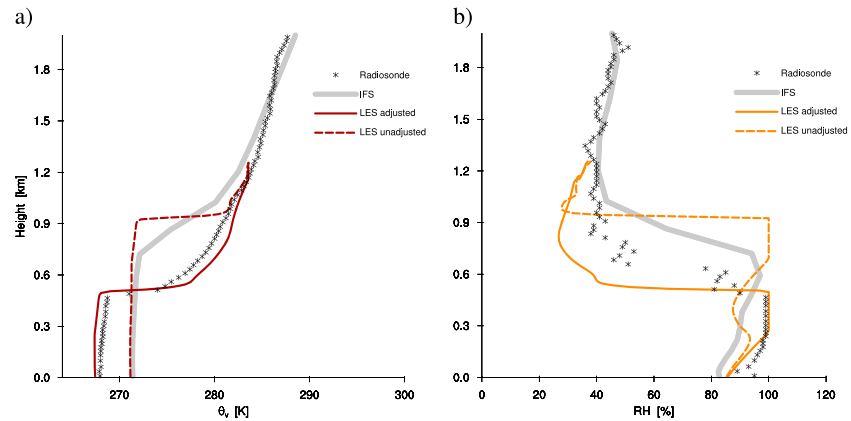


**Figure 6.** Evaluation of the vertical profiles of (a)  $\theta_v$  and (b) RH of the unadjusted and adjusted simulation of the 0704 case at the *Polarstern* time point against the radiosonde data. The IFS profile is also shown, for reference. The unadjusted and adjusted LES experiments correspond to the dot and cross indicated in Figure 5, respectively. RH = relative humidity; IFS = Integrated Forecasting System; LES = large-eddy simulation.

#### 4.1. Microgrids: Two-Point Calibration

The first step is to explore for how long the impacts of initial perturbations survive in the simulations. Figure 4 shows two sensitivity tests for the 0704 case, one for the initial thermal inversion height  $z_i$  and one for the initial low-level temperature  $T_{29}$ , which is interpolated between model levels. What stands out is that the difference in both initial inversion height and temperature are more or less preserved throughout the simulated period. This is an expression of the long memory of the AML for upstream conditions, on time scales that go far beyond the daily. Another feature that catches the eye is the considerable variation in inversion height  $z_i$  throughout the simulated period.

The apparent long memory of initial conditions motivates taking an iterative approach for calibrating the case. First an ensemble of cases is simulated on microgrids, with the initial conditions covering a phase space of  $(\Delta\theta_0, z_{i0})$  values. That phase space is then scanned for the combination that yields the smallest bias for both variables compared to the observed values at the time point of the PS crossing. This technique only works if the downstream bias is a monotonic function of the initial perturbation, for both variables.

The technique is illustrated in Figure 5 for the 0704 case. Using the unadjusted IFS initial state  $(\Delta\theta_0, z_{i0}) = (0\text{K}, 1,000\text{m})$  (indicated by the black dot) yields a bias of  $(+3\text{K}, +400\text{m})$  at the time point of the PS crossing. A cooler initial AML reduces the downstream low-level temperature bias, almost independently of the initial depth  $z_{i0}$ . In contrast, the downstream bias in  $z_i$  is affected by both parameters. While the impact of  $z_{i0}$  can be understood by considering the AML mass budget, the impact of  $\Delta\theta_0$  is explained by the classic flux-jump relation (Canut et al., 2012; Faloon et al., 2005; Lilly, 1968) for the top-entrainment rate  $w_e$  in turbulent mixed layers under an inversion,

$$w_e = -\frac{\overline{w'\theta'_v}|_{z_i}}{\Delta\theta_v}. \quad (1)$$

A cooler initial AML increases the thermal strength of the AML inversion, as measured by the jump  $\Delta\theta_v$  across it. For a given flux  $\overline{w'\theta'_v}|_{z_i}$  this dampens the entrainment rate  $w_e$  through its inverse dependence on  $\Delta\theta_v$ . As a result, the AML deepens less during the simulation and thus reduces the downstream bias in  $z_i$ . This explains why the gradient in the depth bias in Figure 5a is oriented in a diagonal direction. The “best setting” is that combination of  $(\Delta\theta_0, z_{i0})$  for which the bias in both variables is minimal. For the 0704 case this is the combination  $(-3\text{K}, 400\text{m})$ , indicated by the black cross in Figure 5.

Figure 6 intercompares the vertical thermodynamic structure between the IFS, the unadjusted LES and the adjusted LES for the 0704 case. Above the inversion the IFS agrees remarkably well with the observed vertical structure but has a too warm and too deep mixed layer (Sotiropoulou et al., 2016). Not adjusting the initial state causes LES to reproduce the downstream bias of the IFS, the only difference being the stronger inversion. The profiles of the adjusted LES agree much better with the radiosonde observations, not just

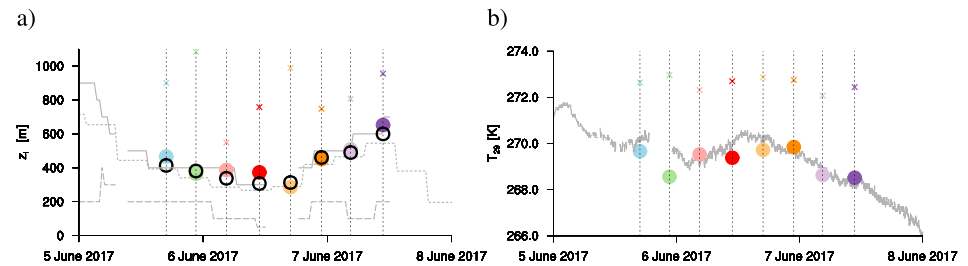


**Figure 7.** Evaluation of the simulated (a) Arctic mixed-layer depth  $z_i$  and (b) low-level temperature  $T_{29}$  at the time point of the PS crossing, for all eight trajectories (colored dots) against PS measurements (open black dots) for all eight cases. The time points of the PS crossing are indicated by the vertical dashed lines. The small colored crosses indicate the results for the unadjusted simulations, for reference. In (a) the horizontal gray lines represent observations of cloud top height  $z_t$  (solid gray), cloud base height  $z_b$  (dashed) and thermal inversion height  $z_i$  (dotted gray). In (b) the observed low-level temperature  $T_{29}$  is shown (solid gray). PS = *Polarstern*.

concerning the depth and temperature of the AML but also concerning the position of the cloud layer (where  $RH \geq 100\%$ ). This result is nontrivial, as clouds are free to develop. Above the inversion the LES has a slight dry bias in this case, which we speculate can be due to (i) uncertainties in the forcing and (ii) the use of a centered-difference scheme.

The calibration procedure described above is applied to all eight cases. The results are summarized in Figure 7, comparing the simulated inversion height and low-level temperature of both the unadjusted and adjusted configurations to the PS observations for all cases. While the biases of the unadjusted simulations are significant and persistent for all eight cases, the adjusted simulations show a satisfactory match for both variables, also reproducing the observed time variation during the 2-day period that is covered. This suggests that the iterative procedure for adjusting the initial state is persistently effective in minimizing the bias in these conditions.

#### 4.2. Microgrids: Eight-Point Evaluation

The next step is to confront the microgrid simulations with other PASCAL observations, independent from the two state variables used for the case calibration. The number of variables used to this purpose is determined by both data availability and relevance. Our goal is to use as many independent variables as possible, more or less representing a “multipoint check” of the simulations. This evaluation strategy at observational sites was recently explored by Neggers and Siebesma (2013) for evaluating a convective boundary layer scheme at a midlatitude permanent meteorological site.

Figure 8 shows the evaluation against eight observed data sets. The first four reflect the mean thermodynamic and kinematic state of the AML, including surface pressure, relative humidity, wind speed, and wind direction. A good agreement with observed pressure is obtained, showing that the IFS forcings capture the local synoptic situation to a satisfactory degree. The near-surface relative humidity is slightly underestimated. The low-level wind speed partially reflects the IFS forcing, but also the resolved momentum transport in the LES. While the speed is reasonable, a slight offset exists in the wind direction, which might be related to differences in the assumed and actual aerodynamic roughness lengths. This behavior might be improved by adopting observed roughness lengths; we consider this case optimization a future research effort.

The next three panels evaluate the state of mixed-phase clouds in the simulations. To this purpose the observed maximum liquid and ice content are used, as these variables can relatively easily be measured, and avoids the problem with vertical integrated water paths in case the cloud base is very low and the lower cloud mass is not captured by the remote sensing instruments. The results indicate that LES reproduces both the liquid and ice maximum water contents to a reasonable degree; in addition, their ratio is representative. The observed very low liquid cloud base height on 6 June is also reproduced, although a slight overestimation exists, which is consistent with the somewhat underestimated RH.

The final panel evaluates the downward short wave radiative flux at the surface, which is another independent indicator of cloud presence. It features a strong diurnal cycle, remaining nonzero overnight. LES generally reproduces this diurnal cycle but also includes considerable deviations. These deviations are not persistently positive or negative. These deviations can reflect differences in cloud presence but also possible inconsistencies between the sampling in the model and in nature; for example, three-dimensional

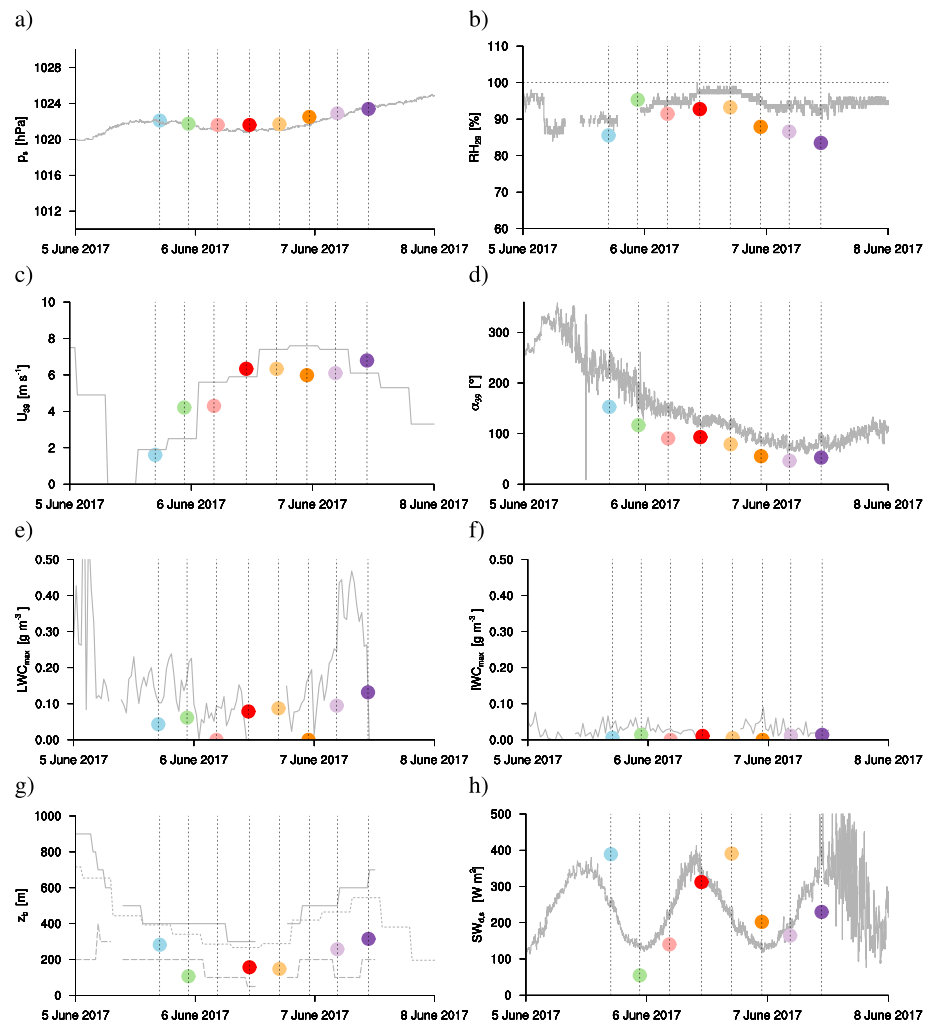


**Figure 8.** Same as Figure 7 but now showing eight other independent atmospheric properties: (a) surface air pressure  $p_s$ , (b) relative humidity  $RH_{29}$ , (c) wind speed  $U_{39}$ , (d) wind direction  $\alpha_{39}$ , (e) maximum liquid water content  $LWC_{max}$ , (f) maximum ice water content  $IWC_{max}$ , (g) liquid cloud base height  $z_b$ , and (h) short-wave downward radiation at the surface  $SW_d$ . The observational data in panels (c) and (g) were gridded. The gray lines in panel (g) are explained in the caption of Figure 7a.

radiative effects are not represented in the LES, which can be important at low zenith angles. Elucidating these differences requires further research.

We conclude from these results that calibrating against observations of two state variables leads to reasonable performance against a further eight independent ones. The fact that the freely developing mixed-phase clouds also agree reasonably well with the observations downstream is encouraging. Even though the match with the observations is sometimes not perfect, the results indicate that the set of Lagrangian cases do represent the observed conditions in general and thus form a suitable virtual database for investigation of what controls the evolution of the cloudy AML in the Arctic.

### 4.3. Macrogrids: AML Evolution

Now that satisfactory agreement with observed bulk thermodynamic, kinematic, and cloudy state of AML has been demonstrated, the next step is to focus on the evolution of the air mass in transition. The eight cases, all slightly different in their evolution, provide a parameter space wide enough for exploring how such transitions take place, also at (resolved) process level. From this point onward the simulations on macrogrids will be used, which in essence do not deviate substantially from the simulations on microgrids. The sensitivity to grid size and discretization is analyzed in detail in Appendix A.

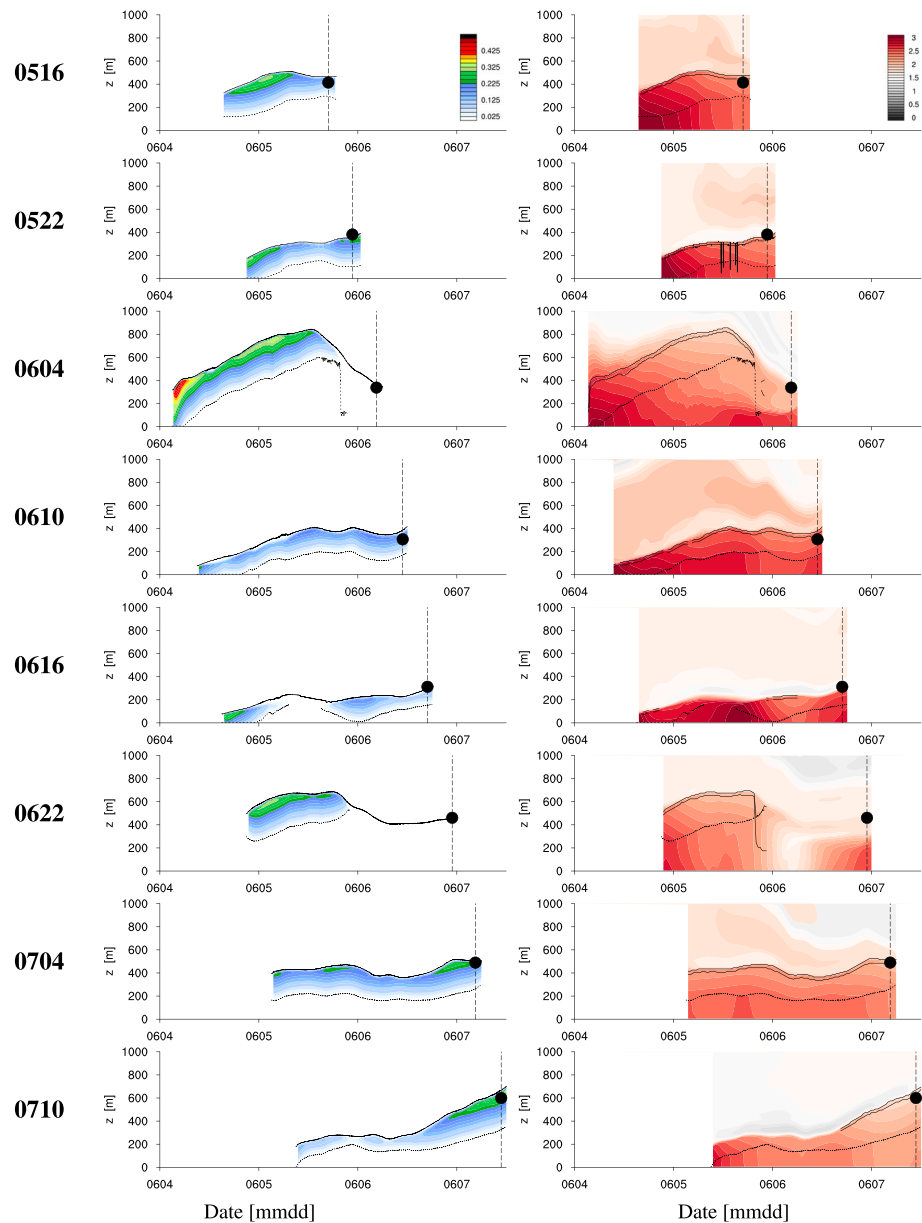


**Figure 9.** Time-height contour plots for all eight simulated cases of liquid cloud condensate  $q_l$  (g/kg, left column) and water vapor specific humidity  $q_v$  (g/kg, right column). The case ID is given on the left. In the cloud liquid water plots the solid black line indicates the thermal inversion height  $z_i$ , while for water vapor it indicates the lower and upper boundary of the capping humidity layer. Liquid cloud base height is always indicated by the dotted black line. The vertical dashed line indicates the time point of the *Polarstern* crossing, with the black dot indicating the observed thermal inversion height  $z_i$ .

Figure 9 shows the evolution of liquid cloud condensate and water vapor specific humidity in the full macrogrid simulations of all eight cases. All cases feature strong time evolution in AML depth during the investigated period, with  $z_i$  covering the range between 100 and 900 m. Another feature for these cases that stands out is the parallel rise of cloud base and cloud top during periods of strong AML deepening, so that cloud depth remains more or less constant. While most cases stay cloudy, some experience cloud collapse (0604, 0616, and 0622). For the 0604 and 0622 cases these collapses occur quite abruptly, within a few hours. After this event the AML has not managed to recover and form clouds before its arrival at the PS. At least for the 0604 case this is in contrast with the cloud observations shown in Figure 8. A feature shared by these collapsing cases is a prolonged period of strong deepening preceding the collapse and a short burst of rapid shallowing during the collapse.

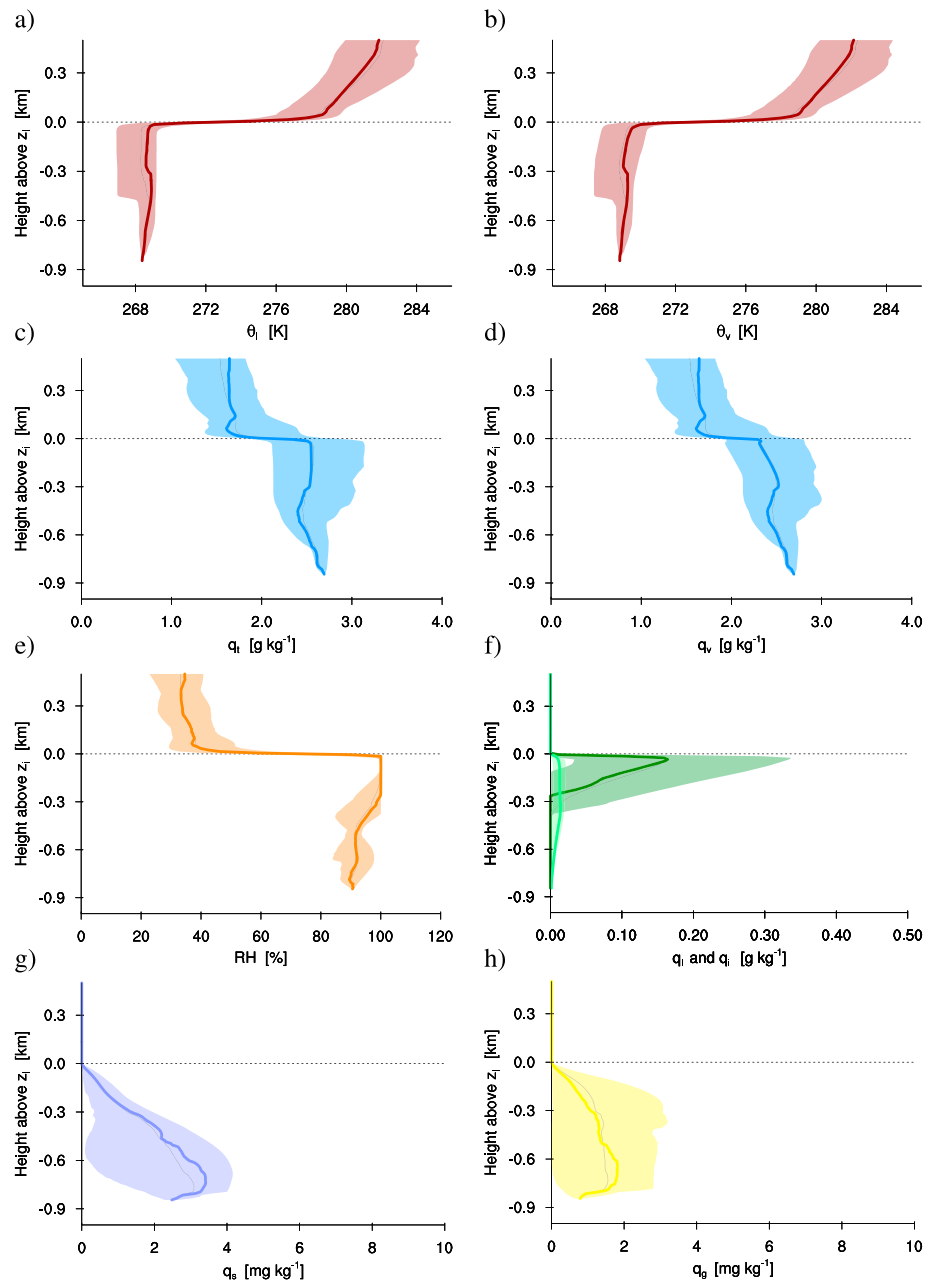


**Figure 10.** Eight-case composite profiles of (a) liquid water potential temperature  $\theta_l$ , (b) virtual potential temperature  $\theta_v$ , (c) total specific humidity  $q_t$ , (d) water vapor specific humidity  $q_v$ , (e) relative humidity RH, (f) liquid and frozen cloud condensate  $q_l$  (dark green) and  $q_i$  (light green), (g) snow  $q_s$ , and (h) graupel  $q_g$ . The last two panels are plotted in milligrams per kilogram, for visualization. Liquid precipitation  $q_r$  is negligible in these experiments. Thick lines represent medians, while the shaded area covers the range between the 5th and 95th percentiles. The average is shown as a thin gray line, for reference. The profiles are vertically aligned at thermal inversion height  $z_i$ , shown as a thin gray dotted line.

The water vapor plots show that a capping humidity layer does form in all simulations, agreeing with the persistent observation of this feature as shown Figure 2. However, the layer always is too shallow, with depths of 50 m at most. Note that the reliability of the measurements of this delicate feature is still a topic of discussion in the literature (Naakka et al., 2018), which also complicates its comparison to LES results. A thorough analysis of this problem is for now considered beyond the scope of this paper.

#### 4.4. Macrogrids: Composite Vertical Structure

Multicase composite profiles are now calculated to investigate the vertical structure of the AML. Composites are adopted to make full use of the enhanced statistical significance provided by this set of eight different scenarios. The composites are based on all time points in all eight simulated trajectories, consisting of domain- and time-averaged profiles sampled every 1,800 s. Periods without liquid cloud occurrence are excluded, to better focus on the vertical structure in the mixed-phase cloud-covered AML. In the composite calculation all vertical profiles are vertically aligned at the thermal inversion height  $z_i$ . The purpose of this axis transformation is to focus on behavior at and above the thermal inversion, a choice motivated by the fact that AML turbulence is predominantly driven by cloud top cooling in these conditions.

Figures 10a–10d show that the composite thermodynamic structure of the AML exhibits the typical structure of weakly coupled cloudy mixed layers in the summertime Arctic (Brooks et al., 2017; Shupe et al., 2013). It is dominated by a strong capping inversion, featuring median jumps of about +9 K in temperature and  $-1$  g/kg in total specific humidity across a very shallow layer. A well mixed cloud layer of about 300 m depth is situated below, while above the free troposphere is statically stable but still contains significant humidity, at values of about half the below-inversion state. Note that in this respect the cases are different from the idealized control case of Solomon et al. (2014), which featured much higher humidity above the cloud layer. The composite mixed layer is only weakly coupled to the surface, as testified by a local maximum in  $\theta_l$  and  $\theta_v$  and a local minimum in  $q_v$  below the cloud layer.

The mixed-phase clouds in these realizations shown in Figures 10e–10h reside in a layer with 100% relative humidity, decreasing below cloud base to about 90% at the surface. The liquid cloud condensate carries the typical triangular vertical structure typical of stratocumulus-topped mixed layers, reflecting the adiabatic increase of LWC with height. The fact that this shape still appears in the composite median over many different cloud depths reflects that this shape is persistent in all cases. Ice condensate is much smaller in amplitude, peaking below liquid cloud base but reaching all the way to the surface. The composite liquid-ice partitioning reflects the evaluation results in Figures 8e and 8f and is in agreement with the observations in this respect. Liquid precipitation is negligible, while frozen precipitation gradually increases toward the surface.

The thin capping humidity layers visible in Figure 9 barely show up in the composite water vapor profile in Figure 10d. This reflects that this feature does not always occur in the simulations and is underestimated in amplitude. Apparently, the conditions are right in this experiment setup for its genesis but do not favor its full development. Previous research has provided insight into such humidity inversions, revealing that they tend to form when precipitation removes humidity from an internal mixed layer while the residual layer above remains unchanged (Tjernström et al., 2015, 2019). Decoupling from humidity sources above and below can help in this process (Loewe et al., 2017; Solomon et al., 2011, 2014). Given these insights we speculate that the supply of humidity into the mixed layer in our experiments is just weak enough for such inversions to start forming but on the other hand just strong enough to prevent eventual cloud disappearance and AML collapse. Another possible reason is that the large-scale forcing derived from the GCM complicates the formation of humidity inversions in the simulations, because GCMs do not satisfactorily reproduce these phenomena (Sotiropoulou et al., 2016).

#### 4.5. Macrogrids: Composite Budgets

LES has the advantage that it provides full four-dimensional information on small scale processes that, together with the forcing, are responsible for the way in which the simulated AML evolves. The next step is therefore to perform a detailed budget analysis of prognostic variables reflecting the thermodynamic state and bulk mass of the AML. These analyses are designed to provide more information on the relative roles of local and remotely controlled processes.

##### 4.5.1. Thermodynamics

The prognostic budget of  $\phi \in \{\theta_l, q_l\}$  in the LES can in simple form be written as a sum of individual tendencies,

$$\frac{\partial \phi}{\partial t} = \text{Tr}_\phi + \mu_\phi + R_\phi + F_\phi, \quad (2)$$

where tendency  $\text{Tr}$  stands for the combined subgrid and resolved transport in the LES,  $\mu$  represents microphysical effects,  $R$  represents net radiation, and  $F$  is the impact of the prescribed large-scale forcing. Figure 11

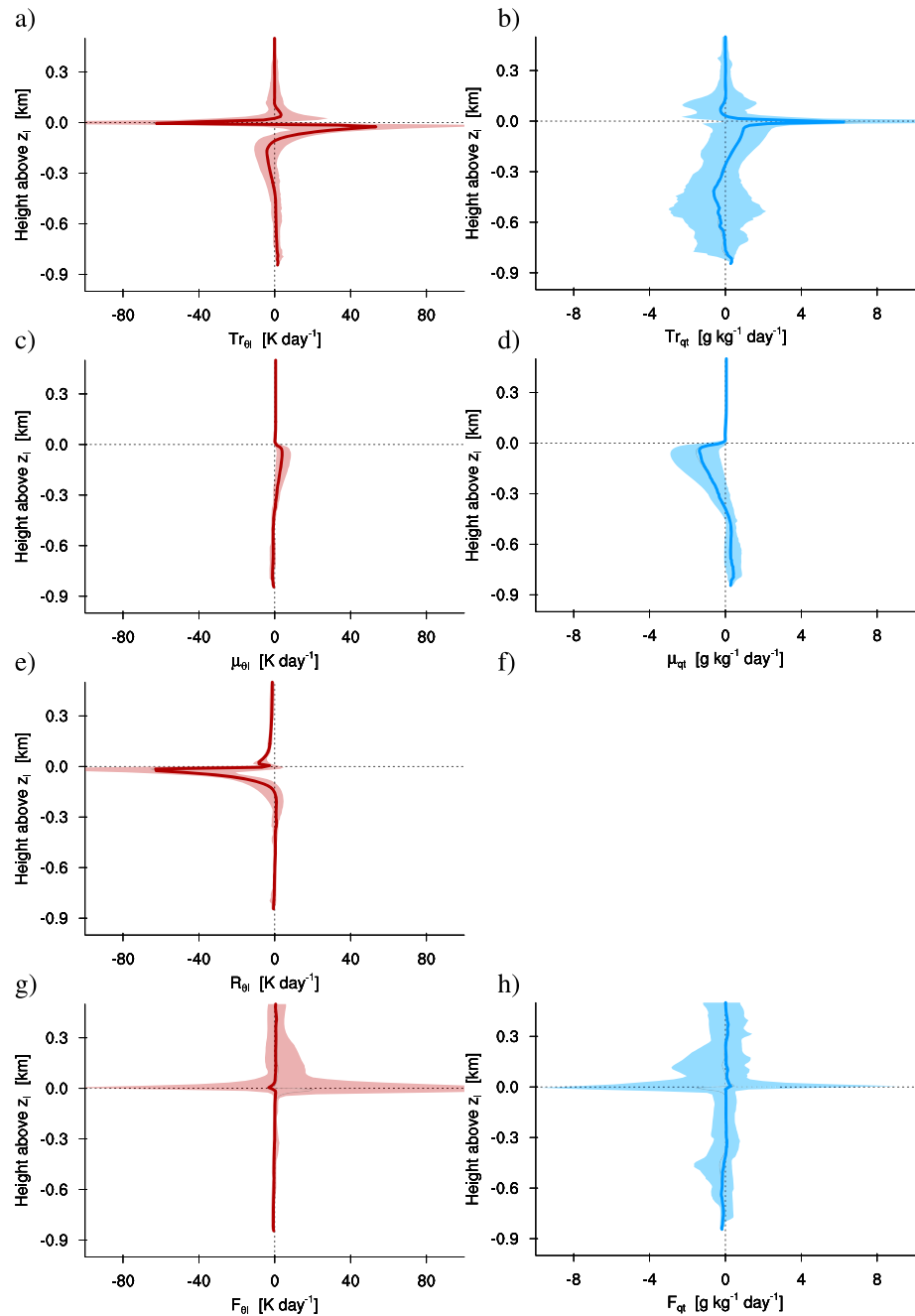


**Figure 11.** Composite budgets of  $\theta_l$  (red, left column) and  $q_l$  (blue, right column). Each panel shows the vertical profiles of single budget terms: resolved and subgrid transport  $Tr$  (a and b), microphysics  $\mu$  (c and d), radiation  $R$  (e), and large-scale forcing  $F$  (g and h) including both horizontal and vertical advection. The profiles are vertically aligned at inversion height  $z_i$ , shown as a thin gray dotted line.

shows composite profiles of the most important terms in (2). For better interpreting these results a distinction is made between the (i) AML-internal behavior and (ii) the behavior at inversion-level.

The AML internal  $\theta_l$  budget is dominated by three terms: (i) radiative cooling (Figure 11e), (ii) turbulent transport (Figure 11a), and (iii) the impacts of microphysics (Figure 11c). Cloud top cooling is the dominant sink for about 100 m below the inversion, peaking immediately below at values that are comparable to those observed during PASCAL (Wendisch et al., 2018) but also during other recent field campaigns (Brooks et al., 2017). This cooling is roughly balanced by the combined heating effect of turbulent transport and precipitation formation. Turbulence continuously tries to overturn the created instability by transporting heat from

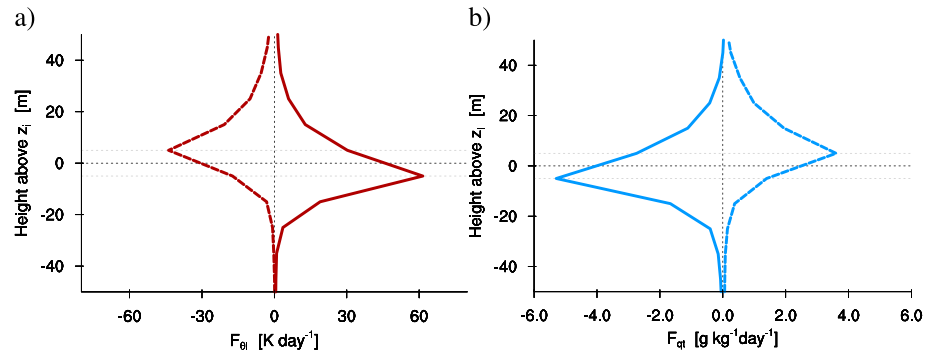


**Figure 12.** Same as Figure 11 but now showing the median composite large-scale forcing tendencies of (a)  $\theta_l$  (red) and (b)  $q_l$  (blue) as conditionally sampled on subsidence (solid line) and upsidence (dashed line) at inversion height  $z_i$ . The plotted height range is adjusted to zoom in on behavior in proximity to the inversion level (horizontal dotted black) and the adjacent levels (dotted gray).

below and above, while precipitation formation effectively acts a source term of  $\theta_l$  (being conserved for condensation of cloud droplets and ice crystals but not for precipitation formation). At about 100 m below the inversion the cloud top cooling has weakened considerably, below which a rough balance exists between precipitation warming and transport cooling. At about 500 m below the inversion the microphysics term turns slightly negative, reflecting the cooling effect of evaporation.

For humidity the AML internal balance consists of microphysics draining humidity from the 300-m-deep cloud layer (Figure 11d), with turbulent transport resupplying humidity from below (Figure 11b). Below cloud base the evaporation of precipitation acts as a small humidity source, again being roughly balanced by turbulent transport. For both heat and moisture the large-scale forcing does not contribute significantly to the composite AML-deep budget.

Near the inversion level the budget is different. At this level the large-scale forcing plays a much bigger role (Figures 11g and 11h), having a small median but showing strong variability. This indicates the occurrence of strong tendencies both negative and positive, which in this Lagrangian setup is likely related to fluctuations in large-scale subsidence. Turbulent transport always cools and moistens the inversion level, thus counteracting the warming and drying effect of both cloud-top entrainment and large-scale subsidence. Cloud-related impacts on the budget at this level, including both microphysics and radiative cooling, are very small due to the locally small cloud condensate amount (also visible in Figure 10f).

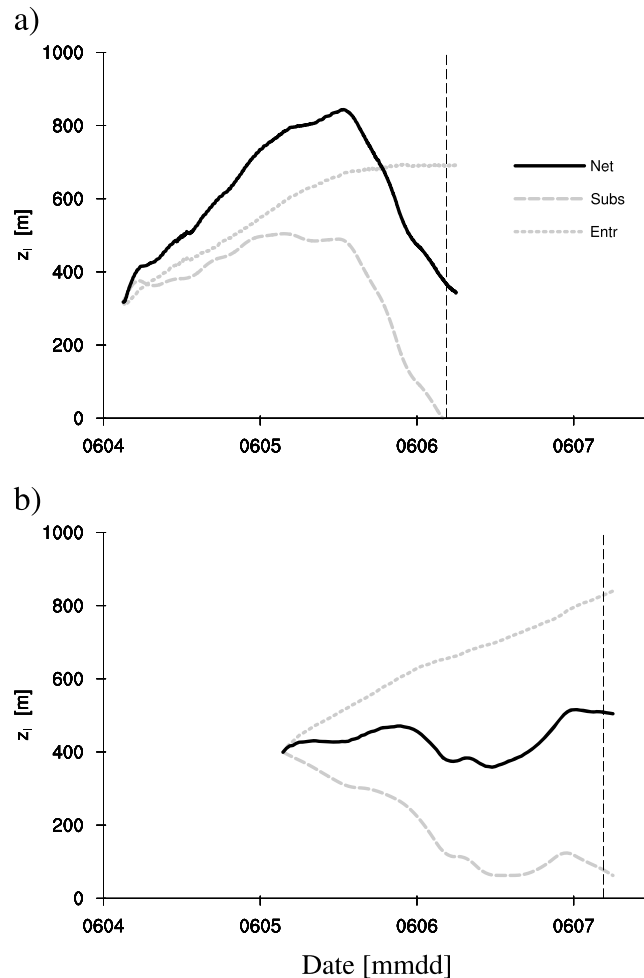
While the basic behavior of the AML-internal heat and humidity budgets as reported here is in line with previous budget studies of Arctic mixed layers, the peculiar role of large-scale subsidence at the inversion level has not been reported before. In particular the occurrence of strong tendencies that are both negative and positive is something new, which is directly related to our choice of maintaining time dependence in the prescribed large-scale forcing. The Lagrangian framework excludes large-scale horizontal advection as a source, so that vertical advection is the only remaining process that can generate these signals. To gain more insight, two new composites are now calculated, one reflecting pure subsidence conditions (i.e.,  $\Omega > 0$ ) at  $z_i$  and the other reflecting pure “upsidence” conditions ( $\Omega < 0$ ).

Figure 12 zooms in on the model levels surrounding the inversion. Both the subsidence and upsidence composite tendencies now have large median amplitudes near the inversion, at values comparable to the other budget terms shown in Figure 11. The signal for subsidence conditions is opposite to the one for upsidence, with heating (cooling) and drying (moistening) during subsidence (upsidence) conditions. A key difference is that for upsidence the tendencies peak *above* the inversion level, while for subsidence they peak *below* it. During subsidence the AML below the inversion warms and dries, while during upsidence the air above the inversion moistens and cools. This is how the prescribed large-scale vertical velocity effectively modifies the inversion height in a discretized model.

#### 4.5.2. Mass

The prognostic budget of the mass of the AML inside a column of air can be written as

$$\frac{\partial z_i}{\partial t} = w_e + w_{LS}, \quad (3)$$



**Figure 13.** Time integration of all three terms in the bulk Arctic mixed-layer mass budget (3) as a function of the time elapsed since initialization, for the (a) 0604 case and (b) 0704 case. Shown are the net deepening rate  $\partial_t z_i$  (“Net”, black), the large-scale vertical velocity  $w_{LS}$  (“Subs,” dashed gray), and the entrainment rate  $w_e$  (“Entr,” dotted gray). Each term is initialized by  $z_{i0}$ .

where  $w_{LS}$  stands for the large-scale vertical velocity in height coordinates. Top entrainment,  $w_e$ , is generally positive definite and always acts to increase mass and deepen the AML. In contrast,  $w_{LS}$  can be both positive and negative, as encountered in the previous section. In case of subsidence, mass is removed from the column through the associated low-level divergence.

To better understand the role of entrainment (a locally driven process) versus subsidence (a remotely controlled process), the contributions by both to the mass budget are compared in Figure 13. Both terms are diagnosed in the LES at height  $z_i$ , with the entrainment rate calculated using the flux-jump relation (1) depending on the resolved buoyancy flux. All individual terms in (3) are time integrated from initialization, starting with  $z_{i0}$ . As a result, its evolution represents the theoretical scenario of what would happen with the AML depth in case of only one process acting. This is done for two different cases, one (0704) completely cloudy and the other (0604) featuring a sudden cloud collapse. Both cases show that entrainment, being positive definite, is responsible for a gradual and continuous AML deepening. It is relatively constant as long as liquid clouds are present; if clouds disappear, turbulence dies and the entrainment contribution to deepening reduces to 0. In contrast, the contribution by large-scale subsidence is much more variable and can also be negative. Subsidence is thus responsible for the time evolution on short time scales in the net deepening rate, being exclusively responsible for shallowing events.

The picture emerges that strong subsidence events are associated with AML cloud collapse. To quantify this result further, all cases are again combined. Figure 14 shows scatterplots between the effective deepening

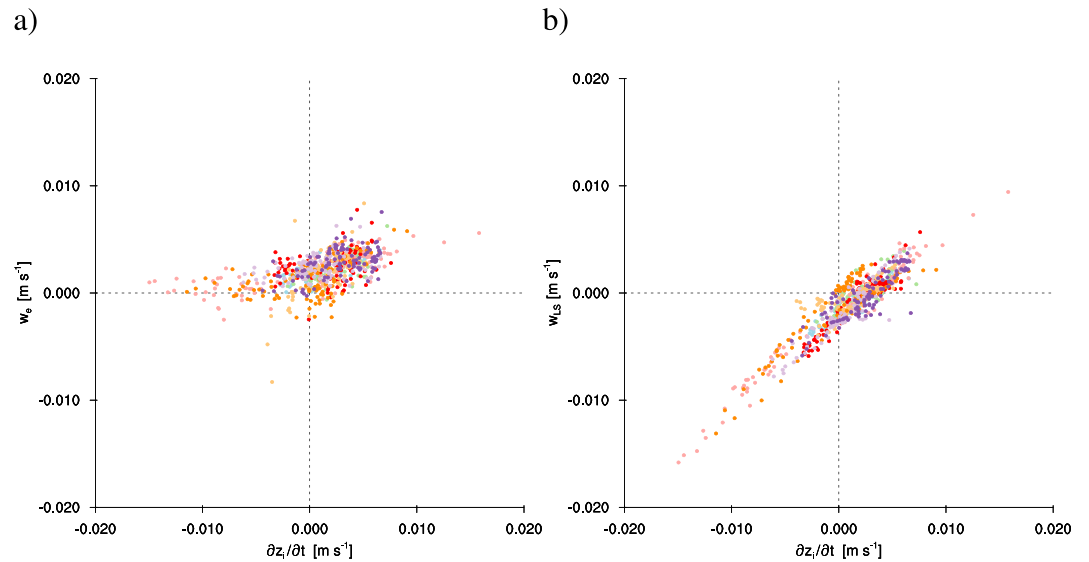


**Figure 14.** Scatterplot of individual terms in bulk AML mass budget (3), showing the effective AML deepening rate  $\partial_i z_i$  versus (a) top entrainment velocity  $w_e$  and (b) large-scale subsidence  $w_{LS}$ . Each dot represents a half-hour mean, its color representing the case as labelled in Figure 2. AML = Arctic mixed layer.

rate on the left-hand side of (3) versus both terms on the right. While the entrainment rate correlates well with the change in  $z_i$  in case of deepening (top right quadrant), this is not so for shallowing (bottom left quadrant). This reflects that entrainment, by definition, deepens the mixed layer. However, the  $z_i$  change correlates much more strongly with large-scale vertical velocity  $w_{LS}$ , in both quadrants. Apparently,  $w_{LS}$  effectively controls the time evolution of  $z_i$ . In addition, it shows that significant subsidence events do occur during the investigated period.

Figure 15 further documents the link between liquid water path (LWP) and subsidence. In the two cases that feature a complete cloud collapse (0604 and 0622) the fatal downward excursion in LWP from the initial equilibrium value of about  $60 \text{ g/m}^2$  is accompanied by a temporary strong increase in the subsidence rate. The associated impact of cloud collapse on the surface radiative budget is also significant, featuring a

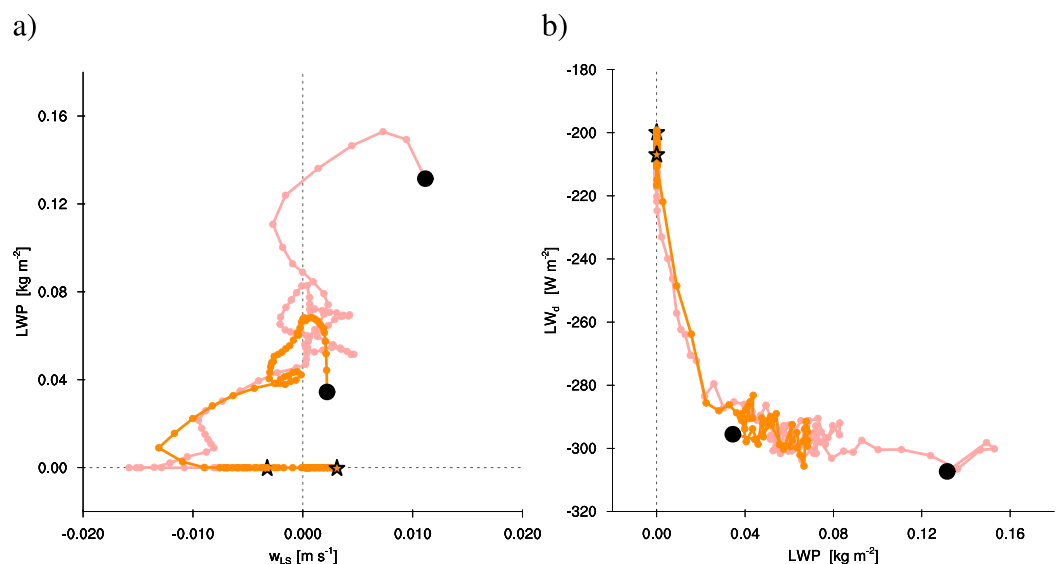


**Figure 15.** Similar to Figure 14 but now showing (a) LWP versus  $w_{LS}$  and (b) LWP versus the surface downward longwave radiative flux  $LW_d$  (negative downward) for the two cases that featured a complete cloud collapse (0604 in salmon and 0622 in orange). The start and end of each trajectory are indicated by the thick black dot and star, respectively. LWP = liquid water path.

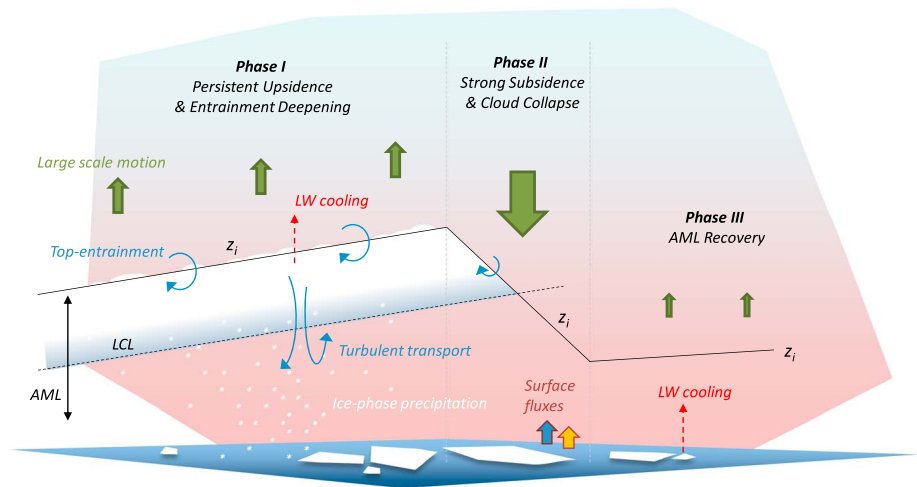


**Figure 16.** Schematic illustration of the sequence of processes leading up to a subsidence-induced cloud collapse, as explained in section 5. The green arrows indicate large-scale vertical velocity, while the blue arrows indicate turbulent motions. The red arrows stand for longwave radiative cooling. LCL = lifting condensation level; AML = Arctic mixed layer; LW = longwave.

reduction in the surface longwave downward flux by up to  $100 \text{ W/m}^2$ . Such changes in radiative flux are in line with previous studies on the impact of low-level Arctic clouds on the surface energy budget and the associated melt of sea ice (Bennartz et al., 2012; Kapsch et al., 2016).

## 5. Discussion

The main purpose of this study was to gain insight into the relative role of locally driven processes versus remotely controlled processes in the effective evolution of the AML, in particular concerning cloud amount. The results obtained single out the importance of strong large-scale subsidence events, as these have the potential to cause cloud collapse.

A conceptual model explaining this process is schematically illustrated in Figure 16. Phase I consists of mixed-phase clouds under persistent upsidence conditions. The turbulence generated by cloud top cooling continuously entrains warm and dry air from above the thermal inversion into the AML. This process in itself drives a rise in the LCL. When the LCL rise is comparable to the effective deepening rate, this leads to the cloud layer being lifted as a whole, maintaining its depth (Van der Dussen et al., 2014). This parallel rise can take place when entrainment deepening coincides with upsidence deepening, which for example, happens in the 0604 and 0622 cases (see Figures 9 and 13a). However, when upsidence then suddenly changes into strong subsidence, the AML depth decreases abruptly (phase II). LCL does not have enough time to adjust and sink at an equal rate, simply because radiation and surface evaporation are not capable of cooling and moistening the AML quickly enough. As a result, the AML top (i.e., the thermal inversion) sinks below LCL and the cloud layer disappears. As soon as subsidence weakens again the AML can start to recover, for example, through surface coupling (phase III).

The results highlight the important role of large-scale subsidence in the Arctic climate system. First, sudden changes in large-scale vertical velocity can apparently break the AML system out of a “slow-manifold” state dominated by cloud-top cooling driven entrainment (Bretherton et al., 2010). Second, subsidence represents a link between local small-scale processes acting in an air mass and larger-scale dynamics controlled by the remote midlatitudes. It is interesting to interpret this in the context of the findings of Stramler et al. (2011) and Morrison et al. (2012), reporting strong correlations between surface pressure and cloud and cloud-free states. This study gives further insight into how transitions between these two dominant states might take place, suggesting that strong subsidence events could play a key role. Once liquid cloud disappears, it might not be that easy to reform it, as mixed-layer forming entrainment also disappears. This means that during these cloud-free periods, the longwave radiative cooling is effectively moved to the surface. More research is needed to fully understand this chain of processes.

Three important simplifications, or rather limitations, were applied in this study. The first concerns the recreation of the upstream state of the air mass. The iterative technique to adjust the initial state as explored in this study goes some way toward addressing the issue of low-level biases in GCMs over the sea ice. In this study the full phase space was covered with microgrid simulations, mainly in order to illustrate the approach and to highlight the long memory of the AML. This procedure could be further optimized, for example, using a convergence method involving fewer simulations. However, independent observations of the upstream state of the air mass are still the best way to constrain the case construction at two ends of the trajectory. This would also allow validation of the reverse-engineering approach explored here.

The second limitation concerns the assumption of a homogeneous surface. While this assumption was applicable for achieving our research objectives, it might prevent the reproduction of some observed delicate features of the AML. The prime example is the capping humidity layer, which does appear in the simulations but often is underestimated. A heterogeneous surface could boost the amplitude and thickness of these capping layers above the thermal inversion, for example, when an air mass crosses a patch of solid ice over which surface evaporation is significantly reduced. Humidity layers created during brief decoupling periods might then be advected around laterally, for example, by wind shear across the thermal inversion. Further research is required to gain insight.

The third limitation concerns the large-scale subsidence, for which the data from only one GCM was used. Subsidence can be very different among GCMs. The apparent importance of subsidence for the mixed-layer evolution thus motivates testing the robustness of this result using alternative estimates of subsidence. One possibility is to derive the large-scale forcings from different GCMs; an alternative is to use observational estimates (Bony et al., 2017).

## 6. Summary, Conclusions and Outlook

In this study Lagrangian LES experiments of transitioning warm air mass intrusions into the high Arctic are constrained by in situ PASCAL observations. The cases are calibrated against two observational data sets and evaluated against a further eight independent data sets. The main results and conclusions of this study can be summarized as follows:

- Significant low-level biases over the sea ice are identified in the GCM data used to drive the LES, which is in line with previous studies;
- An iterative reverse-engineering procedure is explored to address this problem, which relies on LES on microgrids and makes use of the long memory of Arctic air masses of upstream conditions;
- The simulated mixed-phase cloud layers are only weakly coupled to the surface and feature shallow capping humidity layers.
- All eight simulated air masses exhibit a strong time evolution across a range of time scales, including diurnal but also synoptic fingerprints.
- A few cases experience rapid cloud collapse, coinciding with a rapid decrease in AML depth. These events typically occur after a relatively long period of gradual persistent deepening.
- Budget analyses show that turbulent transport counteracts cloud-top radiative cooling and precipitation formation in the AML interior. In the proximity of the thermal inversion the large-scale vertical advection is a major player, showing a distinct difference between subsidence and upsidence conditions.
- AML deepening through entrainment behaves almost time-constantly, as long as clouds are present. In contrast, large-scale subsidence fluctuates strongly and is highly correlated with the net evolution of the inversion height.
- Relatively strong and sudden subsidence events are found to be responsible for the cloud collapses. These collapses substantially reduce the downward longwave radiative flux at the surface, effectively moving the radiative cooling from cloud top to the surface.

The results of this study could inform the objectives and designs of future field campaigns in the Arctic. Concerning the objectives, reliable information on both surface properties and upstream states are here identified as “missing links” in fully understanding observed and simulated cloud transitions. Second, large-scale subsidence is identified as a major player in this process, in particular its role in counteracting entrainment deepening and its potential to cause cloud collapse. Third, the obtained results highlight the benefits of moving away from single-case studies toward a more statistically significant, multiday approach for studying cloud transitions in air masses (Neggers et al., 2017).

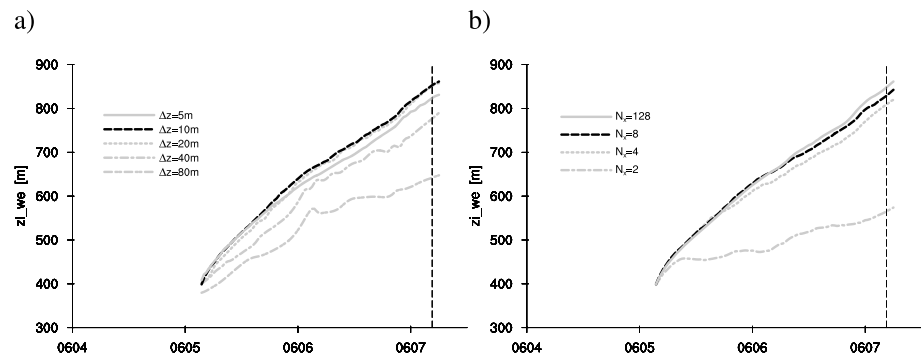


**Figure A1.** Sensitivity of the time-integrated top-entrainment rate in the 0704 case to (a) vertical discretization  $\Delta z$  and (b) horizontal grid size  $N_x = N_y$ . The value highlighted in black is adopted in this study.

The design of such field campaigns should reflect these objectives. For example, dense area-covering surface instrument networks might quantify the average surface heat fluxes and surface heterogeneity across a large area. Tethered balloon measurements some distance above surface can also go some way to fill this data gap, as fluxes at blending height do reflect the surface properties of a larger area. The upstream state of approaching air masses can be probed by either (i) auxiliary sites in a circle around a central site or (ii) long-distance research aircraft or unmanned aerial vehicles. Finally, new techniques recently explored in the subtropics to sample subsidence rates using circles of dropsondes released by long-distance aircraft (Bony et al., 2017) can similarly be applied in the Arctic.

The upcoming MOSAiC field campaign ([www.mosaic-expedition.org](http://www.mosaic-expedition.org)) will probably observe and sample a significant number of warm intrusion events in the Arctic. It thus creates the opportunity to assess how often subsidence-induced cloud collapses occur and how relevant they are for Arctic warming and sea ice melt. To this purpose the authors plan to conduct daily Lagrangian LES during the MOSAiC campaign as part of the ongoing (AC)<sup>3</sup> project, building on the methods developed in this study.

## Appendix A: Sensitivity tests

Figure A1 shows the dependence of the results on the vertical discretization  $\Delta z$  and the horizontal grid size  $N_x = N_y$ . The variable of choice is the time-integrated or cumulative entrainment rate, also used in Figure 13. A weak dependence exists in the range  $40 \text{ m} < \Delta z < 10 \text{ m}$ , with entrainment deepening still becoming a bit more vigorous with resolution. However, the impact significantly diminishes toward  $\Delta z = 10 \text{ m}$ , and the differences below  $10 \text{ m}$  are second order in magnitude. This behavior motivated the adoption of  $\Delta z = 10 \text{ m}$  in this study. Note that although the difference between the 10- and 5-m simulation is small, it is countertrend, probably reflecting an indirect impact on entrainment through cloud condensate.

The sensitivity test for the grid-size  $N_x$  allows interpretation of the representativity of the microgrid configuration (adopted in this study for case calibration) of the macrogrid setup commonly used in most LES studies of cloudy boundary layers. Including only  $2 \times 2$  grid columns significantly underestimates entrainment deepening; however, at  $4 \times 4$  the net entrainment rate is already close to the full macrogrid simulation at  $128 \times 128$  and does not change much anymore at larger grid sizes. This behavior is similar at different horizontal grid spacings (not shown). Based on this result, the  $8 \times 8$  configuration was adopted for the microgrid simulations performed in this study.

## References

- Bennartz, R., Shupe, M., Turner, D., Walden, V., Steffen, K., Cox, C., et al. (2012). Greenland melt extent enhanced by low-level liquid clouds. *Nature*, *496*, 83–86. <https://doi.org/10.1038/nature12002>
- Bony, S., Stevens, B., Ament, F., Bigorre, S., Chazette, P., Crewell, S., et al. (2017). EUREC4A: A field campaign to elucidate the couplings between clouds, convection and circulation. *Surveys in Geophysics*, *38*, 1529–1568. <https://doi.org/10.1007/s10712-017-9428-0>
- Bretherton, C. S., Krueger, S. K., Wyant, M. C., Bechtold, P., Van Meijgaard, E., Stevens, B., & Teixeira, J. (1999). A GCS boundary-layer cloud model intercomparison study of the first ASTEX Lagrangian experiment. *Boundary-Layer Meteorology*, *93*, 341–380. <https://doi.org/10.1023/A:1002005429969>
- Bretherton, C. S., Uchida, J., & Blossey, P. N. (2010). Slow manifolds and multiple equilibria in stratocumulus-capped boundary layers. *Journal of Advances in Modeling Earth Systems*, *2*, 14. <https://doi.org/10.3894/JAMES.2010.2.14>

## Acknowledgments

We thank Ian Brooks and an anonymous reviewer for their informed and constructive comments on this study. The research presented in this paper was supported by the German Research Foundation (Deutsche Forschungsgemeinschaft; DFG) as part of the Transregional Collaborative Research Center “Arctic amplification: Climate relevant atmospheric and surface processes, and feedback mechanisms (AC)<sup>3</sup>” (TRR 172, project 268020496). We further thank the Alfred Wegener Institute (AWI), the PS106/1 crew, and the PASCAL science team for making the field campaign happen. Holger Schmithüsen at the Alfred Wegener Institute (AWI) is acknowledged for processing the surface meteorology and radiosonde data sets from the PASCAL experiment. We thank ECMWF for providing access to the large-scale model analyses and forecasts fields, without which this study would not have been possible. We gratefully acknowledge the Regional Computing Centre of the University of Cologne (RRZK) for granting us access to the CHEOPS cluster. The Gauss Centre for Supercomputing e.V. ([www.gauss-centre.eu](http://www.gauss-centre.eu)) is acknowledged for providing computing time on the GCS Supercomputer JUWELS at the Jülich Supercomputing Centre (JSC) under project no. HKU28. The PASCAL observational data used in this study are publicly accessible on the PANGAEA database, as indicated in Tables 1 and 2. Simulation data including the case configuration and results as used in this publication are available at the website (<https://doi.org/10.5281/zenodo.2573526>).

- Brooks, I. M., Tjernström, M., Persson, P. O. G., Shupe, M. D., Atkinson, R. A., Canut, G., et al. (2017). The turbulent structure of the Arctic summer boundary layer during the Arctic Summer Cloud-Ocean Study. *Journal of Geophysical Research: Atmospheres*, *122*, 9685–9704. <https://doi.org/10.1002/2017JD027234>
- Brunke, M. A., Stegall, S. T., & Zeng, X. (2015). A climatology of tropospheric humidity inversions in five reanalyses. *Atmospheric Research*, *153*, 165–187. <https://doi.org/10.1016/j.atmosres.2014.08.005>
- Canut, G., Couvreux, F., Lothon, M., Pino, D., & Saïd, F. (2012). Observations and large-eddy simulations of entrainment in the sheared Sahelian boundary layer. *Boundary-Layer Meteorology*, *142*, 79–101. <https://doi.org/10.1007/s10546-011-9661-x>
- Curry, J. (1983). On the formation of continental polar air. *Journal of the Atmospheric Sciences*, *40*, 2278–2292.
- Curry, J. A., Hobbs, P. V., King, M. D., Randall, D. A., Minnis, P., Isaac, G. A., et al. (2000). FIRE Arctic Clouds Experiment. *Bulletin of the American Meteorological Society*, *81*(1), 5–30. [https://doi.org/10.1175/1520-0477\(2000\)081<0005:FACE>2.3.CO;2](https://doi.org/10.1175/1520-0477(2000)081<0005:FACE>2.3.CO;2)
- Curry, J. A., Pinto, J. O., Benner, T., & Tschudi, M. (1997). Evolution of the cloudy boundary layer during the autumnal freezing of the Beaufort Sea. *Journal of Geophysical Research*, *102*(D12), 13,851–13,860. <https://doi.org/10.1029/96JD03089>
- Curry, J. A., Schramm, J. L., Rossow, W. B., & Randall, D. (1996). Overview of Arctic cloud and radiation characteristics. *Journal of Climate*, *9*(8), 1731–1764. [https://doi.org/10.1175/1520-0442\(1996\)009<1731:OOACAR>2.0.CO;2](https://doi.org/10.1175/1520-0442(1996)009<1731:OOACAR>2.0.CO;2)
- de Boer, G., Morrison, H., Shupe, M. D., & Hildner, R. (2011). Evidence of liquid dependent ice nucleation in high-latitude stratiform clouds from surface remote sensors. *Geophysical Research Letters*, *38*, L01803. <https://doi.org/10.1029/2010GL046016>
- de Boer, G., Shupe, M. D., Caldwell, P. M., Bauer, S. E., Persson, O., Boyle, J. S., et al. (2014). Near-surface meteorology during the Arctic Summer Cloud Ocean Study (ASCOS): Evaluation of reanalyses and global climate models. *Atmospheric Chemistry and Physics*, *14*(1), 427–445. <https://doi.org/10.5194/acp-14-427-2014>
- de Roode, S. R., Sandu, I., van der Dussen, J. J., Ackerman, A. S., Blossey, P., Jarecka, D., et al. (2016). Large-eddy simulations of EUCLIPSE-GASS Lagrangian stratocumulus-to-cumulus transitions: Mean state, turbulence, and decoupling. *Journal of the Atmospheric Sciences*, *73*(6), 2485–2508. <https://doi.org/10.1175/JAS-D-15-0215.1>
- Faloona, I., Lenschow, D. H., Stevens, B., Campos, T., Blomquist, B., Thornton, D., et al. (2005). *Journal of the Atmospheric Sciences*, *62*, 3268–3285.
- Fridlind, A. M., van Dierenhoven, B., Ackerman, A. S., Avramov, A., Mrowiec, A., Morrison, H., et al. (2012). A FIRE-ACE/SHEBA case study of mixed-phase Arctic boundary layer clouds: Entrainment rate limitations on rapid primary ice nucleation processes. *Journal of the Atmospheric Sciences*, *69*(1), 365–389. <https://doi.org/10.1175/JAS-D-11-052.1>
- Heus, T., Heerwaarden, C. C., Jonker, H. J. J., Siebesma, A. P., Axelsen, S., van den Dries, K., et al. (2010). Formulation of the Dutch Atmospheric Large-Eddy Simulation (DALES) and overview of its applications. *Geoscientific Model Development*, *3*, 415–444. <https://doi.org/10.5194/gmd-3-415-2010>
- Holland, M. M., & Bitz, C. M. (2003). Polar amplification of climate change in coupled models. *Climate Dynamics*, *21*, 221–232. <https://doi.org/10.1007/s00382-003-0332-6>
- Jakobson, E., Vihma, T., Palo, T., Jakobson, L., Keernik, H., & Jaagus, J. (2012). Validation of atmospheric reanalyses over the central Arctic Ocean. *Geophysical Research Letters*, *39*, L10802. <https://doi.org/10.1029/2012GL051591>
- Johansson, E., Devasthale, A., Tjernström, M., Ekman, A. M. L., & L'Ecuyer, T. (2017). Response of the lower troposphere to moisture intrusions into the Arctic. *Geophysical Research Letters*, *44*, 2527–2536. <https://doi.org/10.1002/2017GL072687>
- Kapsch, M.-L., Graverson, R., & Tjernström, M. (2013). Springtime atmospheric energy transport and the control of Arctic summer sea-ice extent. *Nature Climate Change*, *3*, 744–748. <https://doi.org/10.1038/nclimate1884>
- Kapsch, M.-L., Graverson, R. G., Tjernström, M., & Bintanja, R. (2016). The effect of downwelling longwave and shortwave radiation on Arctic summer sea ice. *Journal of Climate*, *29*, 1143–1159.
- Klein, S. A., McCoy, R. B., Morrison, H., Ackerman, A. S., Avramov, A., Boer, G. d., et al. (2009). Intercomparison of model simulations of mixed-phase clouds observed during the ARM Mixed-Phase Arctic Cloud Experiment. I: Single-layer cloud. *Quarterly Journal of the Royal Meteorological Society*, *135*(641), 979–1002. <https://doi.org/10.1002/qj.416>
- Knudsen, E. M., Heinold, B., Dahlke, S., Bozem, H., Crewell, S., Gorodetskaya, I. V., et al. (2018). Meteorological conditions during the ALOUD/PASCAL field campaign near Svalbard in early summer 2017. *Atmospheric Chemistry and Physics*, *18*(24), 17,995–18,022. <https://doi.org/10.5194/acp-18-17995-2018>
- Knust, R. (2017). Polar research and supply vessel Polarstern operated by the Alfred-Wegener-Institute. *Journal of Large-scale Research Facilities*, *3*, A119. <https://doi.org/10.17815/jlsrf-3-163>
- Lilly, D. K. (1968). Models of cloudy-topped mixed layers under a strong inversion. *Quarterly Journal of the Royal Meteorological Society*, *94*, 292–309.
- Lindsay, R., Wensnahan, M., Schweiger, A., & Zhang, J. (2014). Evaluation of seven different atmospheric reanalysis products in the Arctic. *Journal of Climate*, *27*(7), 2588–2606. <https://doi.org/10.1175/JCLI-D-13-00014.1>
- Loewe, K., Ekman, A. M. L., Paukert, M., Sedlar, J., Tjernström, M., & Hoose, C. (2017). Modelling micro- and macrophysical contributors to the dissipation of an Arctic mixed-phase cloud during the Arctic Summer Cloud Ocean Study (ASCOS). *Atmospheric Chemistry and Physics*, *17*(11), 6693–6704. <https://doi.org/10.5194/acp-17-6693-2017>
- Macke, A., & Flores, H. (2018). The Expeditions PS106/1 and 2 of the Research Vessel Polarstern to the Arctic Ocean in 2017. *Reports on Polar and Marine Research, Alfred Wegener Institute (AWI), Bremerhaven, Germany*, *719*, 171. [https://doi.org/10.2312/BzPM\\_0719\\_2018](https://doi.org/10.2312/BzPM_0719_2018)
- Makshtas, A., Atkinson, D., Kulakov, M., Shutilin, S., Krishfield, R., & Proshutinsky, A. (2007). Atmospheric forcing validation for modeling the central Arctic. *Geophysical Research Letters*, *34*, L20706. <https://doi.org/10.1029/2007GL031378>
- McFarquhar, G. M., Ghan, S., Verlinde, J., Korolev, A., Strapp, J. W., Schmid, B., et al. (2011). Indirect and semi-direct aerosol campaign. *Bulletin of the American Meteorological Society*, *92*(2), 183–201. <https://doi.org/10.1175/2010BAMS2935.1>
- Miller, N. B., Shupe, M. D., Cox, C. J., Walden, V. P., Turner, D. D., & Steffen, K. (2015). Cloud radiative forcing at Summit, Greenland. *Journal of Climate*, *28*(15), 6267–6280. <https://doi.org/10.1175/JCLI-D-15-0076.1>
- Morrison, H., de Boer, G., Feingold, G., Harrington, J., Shupe, M. D., & Sulia, K. (2012). Resilience of persistent Arctic mixed-phase clouds. *Nature Geoscience*, *5*, 11–17. <https://doi.org/10.1038/NNGEO1332>
- Morrison, H., Zuidema, P., Ackerman, A. S., Avramov, A., de Boer, G., Fan, J., et al. (2011). Intercomparison of cloud model simulations of Arctic mixed-phase boundary layer clouds observed during SHEBA/FIRE-ACE. *Journal of Advances in Modeling Earth Systems*, *3*, M05001. <https://doi.org/10.1029/2011MS000066>
- Naakka, T., Nygård, T., & Vihma, T. (2018). Arctic humidity inversions: Climatology and processes. *Journal of Climate*, *31*(10), 3765–3787. <https://doi.org/10.1175/JCLI-D-17-0497.1>
- Neggers, R. A. J., Ackerman, A. S., Angevine, W. M., Bazile, E., Beau, I., Blossey, P. N., et al. (2017). Single-column model simulations of subtropical marine boundary-layer cloud transitions under weakening inversions. *Journal of Advances in Modeling Earth Systems*, *9*, 2385–2412. <https://doi.org/10.1002/2017MS001064>

- Neggers, R. A. J., & Siebesma, A. P. (2013). Constraining a system of interacting parameterizations through multiple-parameter evaluation: Tracing a compensating error between cloud vertical structure and cloud overlap. *Journal of Climate*, *26*, 6698–6715. <https://doi.org/10.1175/JCLI-D-12-00779.1>
- Ovchinnikov, M., Ackerman, A. S., Avramov, A., Cheng, A., Fan, J., Fridlind, A. M., et al. (2014). Intercomparison of large-eddy simulations of Arctic mixed-phase clouds: Importance of ice size distribution assumptions. *Journal of Advances in Modeling Earth Systems*, *6*, 223–248. <https://doi.org/10.1002/2013MS000282>
- Ovchinnikov, M., Korolev, A., & Fan, J. (2011). Effects of ice number concentration on dynamics of a shallow mixed-phase stratiform cloud. *Journal of Geophysical Research*, *116*, D00T06. <https://doi.org/10.1029/2011JD015888>
- Pithan, F., Ackerman, A., Angevine, W. M., Hartung, K., Ickes, L., Kelley, M., et al. (2016). Select strengths and biases of models in representing the Arctic winter boundary layer over sea ice: The Larcform 1 single column model intercomparison. *Journal of Advances in Modeling Earth Systems*, *8*, 1345–1357. <https://doi.org/10.1002/2016MS000630>
- Pithan, F., Medeiros, B., & Mauritsen, T. (2014). Mixed-phase clouds cause climate model biases in Arctic wintertime temperature inversions. *Climate Dynamics*, *43*, 289–303.
- Pithan, F., Svensson, G., Caballero, R., Chechin, D., Cronin, T. W., Ekman, A. M. L., et al. (2018). Role of air-mass transformations in exchange between the Arctic and mid-latitudes. *Nature Geoscience*, *11*, 805–812. <https://doi.org/10.1038/s41561-018-0234-1>
- Sandu, I., & Stevens, B. (2011). On the factors modulating the stratocumulus to cumulus transitions. *Journal of the Atmospheric Sciences*, *68*, 1865–1881. <https://doi.org/10.1175/2011JAS3614.1>
- Savre, J., & Ekman, A. M. L. (2015). Large-eddy simulation of three mixed-phase cloud events during ISDAC: Conditions for persistent heterogeneous ice formation. *Journal of Geophysical Research: Atmospheres*, *120*, 7699–7725. <https://doi.org/10.1002/2014JD023006>
- Savre, J., Ekman, A. M. L., Svensson, G., & Tjernström, M. (2015). Large-eddy simulations of an Arctic mixed-phase stratiform cloud observed during ISDAC: Sensitivity to moisture aloft, surface fluxes and large-scale forcing. *Quarterly Journal of the Royal Meteorological Society*, *141*(689), 1177–1190. <https://doi.org/10.1002/qj.2425>
- Sedlar, J., & Tjernström, M. (2017). Clouds, warm air, and a climate cooling signal over the summer Arctic. *Geophysical Research Letters*, *44*, 1095–1103. <https://doi.org/10.1002/2016GL071959>
- Seifert, A., & Beheng, K. D. (2006). A two-moment cloud microphysics parameterization for mixed-phase clouds. Part 1: Model description. *Meteorology and Atmospheric Physics*, *92*, 45–66. <https://doi.org/10.1007/s00703-005-0112-4>
- Shupe, M. D. (2011). Clouds at Arctic atmospheric observatories. Part II: Thermodynamic phase characteristics. *Journal of Applied Meteorology and Climatology*, *50*(3), 645–661. <https://doi.org/10.1175/2010JAMC2468.1>
- Shupe, M. D., Matrosov, S. Y., & Uttal, T. (2006). Arctic mixed-phase cloud properties derived from surface-based sensors at SHEBA. *Journal of the Atmospheric Sciences*, *63*(2), 697–711. <https://doi.org/10.1175/JAS3659.1>
- Shupe, M. D., Persson, P. O. G., Brooks, I. M., Tjernström, M., Sedlar, J., Mauritsen, T., et al. (2013). Cloud and boundary layer interactions over the Arctic sea ice in late summer. *Atmospheric Chemistry and Physics*, *13*(18), 9379–9399. <https://doi.org/10.5194/acp-13-9379-2013>
- Solomon, A., Feingold, G., & Shupe, M. D. (2015). The role of ice nuclei recycling in the maintenance of cloud ice in Arctic mixed-phase stratocumulus. *Atmospheric Chemistry and Physics*, *15*(18), 10,631–10,643. <https://doi.org/10.5194/acp-15-10631-2015>
- Solomon, A., Shupe, M. D., Persson, P. O. G., & Morrison, H. (2011). Moisture and dynamical interactions maintaining decoupled Arctic mixed-phase stratocumulus in the presence of a humidity inversion. *Atmospheric Chemistry and Physics*, *11*(19), 10,127–10,148. <https://doi.org/10.5194/acp-11-10127-2011>
- Solomon, A., Shupe, M. D., Persson, O., Morrison, H., Yamaguchi, T., Caldwell, P. M., & de Boer, G. (2014). The sensitivity of springtime Arctic mixed-phase stratocumulus clouds to surface-layer and cloud-top inversion-layer moisture sources. *Journal of the Atmospheric Sciences*, *71*(2), 574–595. <https://doi.org/10.1175/JAS-D-13-0179.1>
- Sotiropoulou, G., Sedlar, J., Forbes, R., & Tjernström, M. (2016). Summer Arctic clouds in the ECMWF forecast model: An evaluation of cloud parametrization schemes. *Quarterly Journal of the Royal Meteorological Society*, *142*, 387–400. <https://doi.org/10.1002/qj.2658>
- Sotiropoulou, G., Tjernström, M., Savre, J., Ekman, A. M. L., Hartung, K., & Sedlar, J. (2018). Large-eddy simulation of a warm-air advection episode in the summer Arctic. *Quarterly Journal of the Royal Meteorological Society*, *144*(717), 2449–2462. <https://doi.org/10.1002/qj.3316>
- Stramler, K., Del Genio, A., & Rossow, W. (2011). Synoptically driven Arctic winter states. *Journal of Climate*, *24*, 1747–1762.
- Svensson, G., & Karlsson, J. (2011). On the Arctic wintertime climate in global climate models. *Journal of Climate*, *24*, 5757–5771.
- Tan, I., Storelvmo, T., & Zelinka, M. D. (2016). Observational constraints on mixed-phase clouds imply higher climate sensitivity. *Science*, *352*, 224–227. <https://doi.org/10.1126/science.aad5300>
- Tjernström, M., Shupe, M. D., Brooks, I. M., Achtert, P., Prytherch, J., & Sedlar, J. (2019). Arctic summer air mass transformation, surface inversions, and the surface energy budget. *Journal of Climate*, *32*(3), 769–789. <https://doi.org/10.1175/JCLI-D-18-0216.1>
- Tjernström, M., Shupe, M. D., Brooks, I. M., Persson, P. O. G., Prytherch, J., Salisbury, D. J., et al. (2015). Warm-air advection, air mass transformation and fog causes rapid ice melt. *Geophysical Research Letters*, *42*, 5594–5602. <https://doi.org/10.1002/2015GL064373>
- Turner, J. K., & Gyakum, J. R. (2011). The development of Arctic air masses in northwest Canada and their behaviour in a warming climate. *Journal of Climate*, *24*, 4818–4633.
- Van Laar, T. W., Schemann, V., & Neggers, R. A. J. (2019). Investigating the diurnal evolution of the cloud size distribution of continental cumulus convection using multi-day LES. *Journal of the Atmospheric Sciences*, *76*, 729–747. <https://doi.org/10.1175/JAS-D-18-0084.1>
- Van der Dussen, J. J., de Roode, S. R., Ackerman, A. S., Blossey, P. N., Bretherton, C. S., Kurowski, M. J., et al. (2013). The GASS/EUCLIPSE model intercomparison of the stratocumulus transition as observed during ASTEX: LES results. *Journal of Advances in Modeling Earth Systems*, *5*, 483–499. <https://doi.org/10.1002/2013MS000303>
- Van der Dussen, J. J., de Roode, S. R., & Siebesma, A. P. (2014). Factors controlling rapid stratocumulus cloud thinning. *Journal of the Atmospheric Sciences*, *71*(2), 655–664. <https://doi.org/10.1175/JAS-D-13-0114.1>
- Verlinde, J., Harrington, J. Y., McFarquhar, G. M., Yannuzzi, V. T., Avramov, A., Greenberg, S., et al. (2007). The Mixed-Phase Arctic Cloud Experiment. *Bulletin of the American Meteorological Society*, *88*(2), 205–222. <https://doi.org/10.1175/BAMS-88-2-205>
- Wendisch, M., Brückner, M., Burrows, J. P., Crewell, S., Dethloff, K., Ebell, K., et al. (2017). Understanding causes and effects of rapid warming in the Arctic. *Eos*, *98*, 22–26. <https://doi.org/10.1029/2017EO064803>
- Wendisch, M., Macke, A., Ehrlich, A., Lüpkes, C., Mech, M., Chechin, D., et al. (2018). The Arctic cloud puzzle: Using ALOUD/PASCAL multi-platform observations to unravel the role of clouds and aerosol particles in Arctic amplification. *Bulletin of the American Meteorological Society*, *100*, 841–872. <https://doi.org/10.1175/BAMS-D-18-0072.1>
- Wesslén, C., Tjernström, M., Bromwich, D. H., de Boer, G., Ekman, A. M. L., Bai, L.-S., & Wang, S.-H. (2014). The Arctic summer atmosphere: An evaluation of reanalyses using ASCOS data. *Atmospheric Chemistry and Physics*, *14*(5), 2605–2624. <https://doi.org/10.5194/acp-14-2605-2014>
- Westbrook, C. D., & Illingworth, A. J. (2013). The formation of ice in a long-lived supercooled layer cloud. *Quarterly Journal of the Royal Meteorological Society*, *139*(677), 2209–2221. <https://doi.org/10.1002/qj.2096>

- Wexler, H. (1936). Cooling in the lower atmosphere and the structure of polar continental air. *Monthly Weather Review*, *64*, 122–136. [https://doi.org/10.1175/1520-0493\(1936\)64<122:CITLAA>2.0.CO;2](https://doi.org/10.1175/1520-0493(1936)64<122:CITLAA>2.0.CO;2)
- Woods, C., & Caballero, R. (2016). The role of moist intrusions in winter Arctic warming and sea ice decline. *Journal of Climate*, *29*, 4473–4485.
- Woods, C., Caballero, R., & Svensson, G. (2013). Large-scale circulation associated with moisture intrusions into the Arctic during winter. *Geophysical Research Letters*, *40*, 4717–4721. <https://doi.org/10.1002/grl.50912>